# PEX14 acts as the interface linking optineurin to cell type-selective pexophagy

Hongli Li[1], Suyuan Chen[2,3], Zander Claes[4], Celien Lismont[1], Bram Vandewinkel[5], Mohamed A. F. Hussein[1,6], Cláudio F. Costa[1], Dorien Imberechts[7], Yiyang Liu[8], Wim Vandenberghe[7], Steven Verhelst[2,9], Myriam Baes[10], Marc Fransen[1,*]

[1] KU Leuven, Department of Cellular and Molecular Medicine, Laboratory of Peroxisome Biology and Intracellular Communication, 3000 Leuven, Belgium.

[2] Leibniz Institut für Analytische Wissenschaften - ISAS, 44227 Dortmund, Germany.

[3] Max Planck Institute of Molecular Physiology, Department of Chemical Biology, 44227 Dortmund, Germany.

[4] KU Leuven, Department of Cellular and Molecular Medicine, Laboratory of Biosignaling & Therapeutics, 3000 Leuven, Belgium.

[5] KU Leuven, Department of Cellular and Molecular Medicine, Laboratory of Viral Cell Biology and Therapeutics, 3000 Leuven, Belgium.

[6] Department of Biochemistry, Faculty of Pharmacy, Assiut University, 71515 Asyut, Egypt.

[7] KU Leuven, Department of Neurosciences, Laboratory for Parkinson Research, 3000 Leuven, Belgium.

[8] KU Leuven, Department of Human Genetics, Laboratory for Biochemical Neuroendocrinology, 3000 Leuven, Belgium.

[9] KU Leuven, Department of Cellular and Molecular Medicine, Laboratory of Chemical Biology 3000 Leuven, Belgium.

[10] KU Leuven, Department of Pharmaceutical and Pharmacological Sciences, Laboratory of Cell Metabolism, 3000 Leuven, Belgium.

*, Corresponding author (e-mail: marc.fransen@kuleuven.be)

Keywords: peroxisomes; pexophagy; PEX14; optineurin; ubiquitin

## Abstract

Peroxisome degradation, known as pexophagy, is essential for eliminating surplus and dysfunctional peroxisomes, with dysregulation linked to various diseases. Previous research revealed that ectopic expression of optineurin (OPTN), a versatile autophagy adaptor involved in multiple autophagic pathways (e.g., mitophagy, aggrephagy, and xenophagy), triggers pexophagy in HEK-293 cells. However, the underlying mechanism remained elusive. Here, we demonstrate that OPTN-mediated pexophagy is a cell type-specific process. In addition, using proximity labeling, we identified PEX14, a peroxisomal membrane protein, as an OPTN-interacting partner. GFP-Trap analyses confirmed this interaction and revealed that PEX14 and OPTN interact through their respective coiled-coil and C-terminal ubiquitin-binding domains, independently of ubiquitin. Furthermore, our results indicate that the C-terminal half of OPTN-GFP induces pexophagy by oligomerization with endogenous OPTN. Overall, these findings propose PEX14 as a docking factor for OPTN at the peroxisomal membrane, facilitating the connection between peroxisomes and the autophagic membrane scaffold during OPTN-mediated pexophagy.

## Introduction

Macroautophagy (here referred to as autophagy) is a critical cellular process wherein unnecessary or damaged intracellular components are enclosed within double-membrane vesicles, called autophagosomes, and subsequently transported to the lysosomal compartment for degradation and recycling [1]. Acting as a vigilant guardian, autophagy plays a crucial role in maintaining cellular and organismal health by efficiently managing responses to various sources of stress. Impaired autophagy flux can result in the accumulation of dysfunctional organelles, contributing to cellular dysfunction by promoting the buildup of oxidative stress and disrupting essential signaling pathways [2]. One such organelle is the peroxisome, renowned for its pivotal role in cellular lipid and $H_2O_2$ metabolism [3].

In mammals, the autophagic degradation of peroxisomes, known as pexophagy, can occur through different mechanisms [4,5]. For example, a well-characterized pathway involves the recruitment of canonical autophagy adaptors like NBR1 [6,7,8] and SQSTM1 [6,7,9], which target ubiquitinated proteins at the peroxisomal membrane (e.g., PEX5 [8,10] and ABCD3 [11]) and bind to microtubule-associated protein 1A/1B light chain 3B (MAP1LC3/LC3) on the autophagosomal membrane [12]. In addition, under specific environmental conditions (e.g., amino acid starvation), lipidated LC3 (called LC3-II) can be recruited to the peroxisomal membrane in a non-canonical manner through direct interaction with the peroxisomal membrane protein (PMP) PEX14 [13,14]. This PMP, a central player in peroxisomal matrix protein import [15], can also recruit the autophagy-related protein 9A (ATG9A), a phospholipid scramblase whose activity plays a key role in autophagosomal membrane expansion [16], through its interaction with the poly(ADP-ribose) family members tankyrase-1 (TNKS) and tankyrase-2 (TNKS2) [17]. Moreover, HSPA8 has been reported to mediate the translocation of the E3 ligase STUB1 to oxidatively-stressed peroxisomes, leading to their turnover by autophagy [18]. Finally, hypoxia and iron chelation have been reported to promote pexophagy by upregulating BNIP3L/NIX through a mechanism yet to be fully characterized, bypassing ubiquitin priming [19,20]. Alterations in pexophagy flux can lead to diseases, either directly [21,22] or through impairment of other selective autophagy pathways [23].

Recently, we demonstrated that ectopic expression of optineurin (OPTN), a recognized autophagy adaptor involved in targeting depolarized mitochondria, protein aggregates, and intracellular bacterial pathogens [24], induces pexophagy in HEK-293 cells [25]. However, the precise mechanisms underlying this process remain unclear. OPTN contains several structural domains crucial for its involvement in autophagy, including a ubiquitin-binding domain (UBD) and an LC3-interacting region (LIR) [26]. OPTN can also interact with diverse protein aggregates through its C-terminal coiled-coil (CC) domain, independently of ubiquitin [26]. In addition, it employs an unconventional mechanism to initiate mitophagy by interacting with and activating TANK-binding kinase 1 (TBK1), a serine/threonine kinase that directly binds to the phosphoinositide 3-kinase (PI3K) complex [27,28]. Phosphorylation of OPTN by TBK1 increases its affinity for ubiquitin chains and LC3, thereby promoting mitophagy [27]. Furthermore, the LIR-LC3 interaction can drive the ubiquitin-independent recruitment of OPTN, further enhancing mitophagy [29]. OPTN also harbors a leucine zipper (LZ) domain capable of forming a complex with ATG9A vesicles, which initiates the formation of local autophagosomal membranes [30]. Notably, dysfunctions in OPTN-mediated autophagy have been associated with various diseases, including but not limited to amyotrophic lateral sclerosis, glaucoma, and Crohn's disease [24].

In this study, we demonstrate that OPTN functions as a cell type-specific receptor for pexophagy. In addition, through proximity labeling proteomics, we detected PEX14 within the OPTN interactome. Furthermore, we uncovered that the UBD of OPTN (but not ubiquitin binding) and the CC domain of PEX14 are pivotal for their interaction and pexophagy initiation. Collectively, these findings indicate that PEX14 can act as a molecular bridge linking OPTN to pexophagy.

## Results

### Optineurin drives pexophagy in a cell type-specific manner

We recently discovered that both endogenous and GFP-tagged OPTN can localize to peroxisomes in HEK-293 cells and that ectopic expression of OPTN-GFP in these cells can induce pexophagy, even under basal growth conditions [25]. At the start of this study, we observed variations in the induction of pexophagy by OPTN-GFP among different cell types (Extended Data Fig. 1). As anticipated, this phenomenon correlated with the recruitment of OPTN-GFP to peroxisomes, as evidenced by its colocalization with the peroxisomal marker protein mCherry-PTS1, along with a notable decrease in peroxisome count in HEK-293 and HCT116 cells (compare to Fig. 1c), but not in HeLa or CHO cells (Fig. 1a, left panels). In addition, in these cells, when co-expressed with a high-affinity plasma membrane-targeted anti-GFP nanobody (Supplementary Fig. 1), OPTN-GFP promoted the redistribution of peroxisomes to the plasma membrane (Fig. 1a, right panels). Remarkably, ectopic expression of OPTN-GFP in HEK-293 or HCT116 cells consistently induced the formation of OPTN-GFP/peroxisome clusters (Fig. 1b), which were occasionally observed in non-transfected cells as well (Fig. 1c). Further examination via structured illumination microscopy and volume rendering revealed co-clusters of OPTN-GFP and peroxisomes (Fig. 1d). Mitochondria (Extended Data Fig. 2a), the endoplasmic reticulum (Extended Data Fig. 2a), or lysosomes (Extended Data Fig. 2b) did not exhibit similar clustering. Collectively, these findings underscore the cell type-specific recruitment of OPTN to peroxisomes and emphasize its role as a cell type-specific inducer of pexophagy.

### The peroxisomal membrane protein PEX14 is a proximity partner of OPTN

To gain a better understanding of the molecular factors involved in OPTN-mediated pexophagy, we initially conducted a series of proximity-dependent biotin identification (BioID) experiments in HEK-293 cells transiently expressing OPTN-GFP fused to the miniTurbo biotin ligase (Supplementary Fig. 2; Fig. 2a). Upon the addition of biotin to the medium, this fusion protein enables the proximity-dependent covalent biotin labeling of proteins within a 10 nm radius [31]. Subsequently, through streptavidin-based affinity purification of the biotinylated proteins combined with mass spectrometry identification, the neighboring proteins of OPTN can be identified at the molecular level. Among the top-

ranked proteins identified in three independent replicates were TBK1, a well-known interaction partner of OPTN [32], and the peroxisomal membrane protein PEX14 (Fig. 2b). Notably, apart from PEX1 and ACBD5, known for their involvement in pexophagy [33-35], none of the other peroxisomal proteins detected in the BioID sample (e.g., the abundant peroxisomal membrane proteins PXMP2 and PEX11B) exhibited enrichment. This indicates a specific enrichment of PEX14 when compared to other peroxisomal proteins. To validate PEX14 as an interaction partner of OPTN, we conducted a series of GFP-Trap analyses in HEK-293 cells overexpressing OPTN in various ways: transiently (by electroporating cells with an OPTN-encoding mammalian expression plasmid), inducibly (by treating OPTN-GFP Flp-In T-REx 293 cells with doxycycline), and constitutively (by infecting Flp-In T-REx 293 cells with lentivirus), either alone or in combination with ectopically expressed PEX14. These experiments demonstrate that OPTN-GFP interacts with PEX14 (Extended Data Fig. 3). Note that the expression levels of OPTN-GFP are approximately 15 times higher than those of endogenous OPTN (Extended Data Fig. 4).

**The C-terminal half of OPTN is sufficient to bind PEX14 and initiate pexophagy**

Optineurin consists of multiple domains that either interact with various types of cargo or regulate the engulfment of cargo into autophagosomes (Fig. 2a). To gain an initial insight into the OPTN domains responsible for interacting with PEX14 and inducing pexophagy, we co-expressed the N-terminal or C-terminal halves of OPTN, fused to GFP, with PEX14 in HEK-293 cells and conducted GFP-Trap analyses and flow cytometry-based pexophagy assays. From these experiments, it is evident that the C-terminal 361 amino acids of OPTN, which include the ubiquitin-binding domain, are sufficient for binding to PEX14 (Fig. 3a,b) and facilitating pexophagy (Fig. 3c-e). In contrast, the N-terminal 209 amino acids of OPTN, containing the TBK1-, LC3-, and ATG9A-binding domains, show weak binding to PEX14 (Fig. 3a,b) and are insufficient to induce pexophagy (Fig. 3d,e).

**OPTN binds PEX14 and triggers pexophagy via its UBD but in a ubiquitin-independent manner**

To delineate the precise C-terminal domain of OPTN responsible for its interaction with PEX14, we first co-expressed OPTN-GFP fusion proteins with internal deletion of CC2 ($OPTN_{\Delta 295\text{-}360}$-GFP), CC3 ($OPTN_{\Delta 422\text{-}454}$-GFP), UBD ($OPTN_{\Delta 454\text{-}520}$-GFP), or ZF ($OPTN_{\Delta 545\text{-}577}$-GFP) domain, alongside non-tagged full-length PEX14. Results indicate that the deletion of amino

acids 454 to 520, encompassing the full UBD domain, significantly diminishes the affinity of OPTN for PEX14 (Fig. 4a,b). Unfortunately, due to the very low expression levels of $OPTN_{545-577}$-GFP (data not shown), no reliable conclusions could be drawn regarding the potential role of the ZF domain of OPTN in PEX14 binding. To further investigate whether OPTN recognizes PEX14 in a ubiquitin-dependent or ubiquitin-independent manner, we co-expressed PEX14 with $OPTN_{D474N}$-GFP and GFP-$OPTN_{\Delta 474-479}$, two OPTN variants with key residues in the UBD domain mutated or deleted [36,37]. These experiments demonstrate that ubiquitin binding is not necessary for the OPTN-PEX14 interaction (Fig. 4c,d). In addition, all OPTN variants capable of binding PEX14 can induce pexophagy (Fig. 4e,f).

**The C-terminal half of OPTN-GFP triggers pexophagy through oligomerization with endogenous OPTN**

To gain further insight into how a truncated OPTN variant lacking the LC3- and ATG9A-binding domains can induce pexophagy, we explored the possibility of its oligomerization with the endogenous protein, which primarily exists as a trimer under physiological conditions [38]. Therefore, we downregulated the expression levels of endogenous OPTN by transfecting HEK-293 cells with a DsiRNA targeting exon 5, encoding amino acids 57 to 123 (Extended Data Fig. 5). These experiments clearly show that knocking down the expression levels of endogenous OPTN interferes with $OPTN_{217-577}$-GFP-mediated pexophagy (Fig. 5). Regrettably, our GFP-Trap analysis protocol did not enable us to confirm this homomeric interaction because endogenous OPTN and $OPTN_{217-577}$-GFP migrate at comparable positions on SDS-PAGE (Extended Data Fig. 5c). Note also that OPTN depletion does not decrease basal pexophagy, at least under the conditions studied.

**PEX14 interacts with OPTN via its predicted coiled-coil domain**

To delineate the domain on PEX14 responsible for its interaction with OPTN, we conducted GFP-Trap assays on lysates derived from HEK-293 cells co-expressing non-tagged OPTN and various PEX14-GFP variants that impair the protein's N-terminal PEX5/PEX13/PEX19-binding domain ($PEX14_{65-377}$-GFP), membrane anchoring region ($PEX14_{\Delta 110-126}$-GFP), PEX14-binding coiled-coil domain ($PEX14_{\Delta 139-199}$-GFP), or C-terminal D/E-rich region ($PEX14_{1-313}$-GFP) [39]. From these experiments, it becomes evident that the homodimerization domain of PEX14 is also essential for its binding to OPTN (Fig. 6a,b). In line with this, co-expression of non-

tagged full-length OPTN with PEX14$_{1-377}$-GFP, but not PEX14$_{\Delta 139-199}$-GFP (or expression of PEX14$_{1-377}$-GFP alone), augmented OPTN-induced pexophagy (Fig. 6c-f).

**AlphaFold2 predictions and molecular dynamics simulations support the complex formation between OPTN and PEX14**

To gain further insight into the complex formation between OPTN and PEX14, we conducted AlphaFold2 (AF2) predictions and molecular dynamics (MD) simulations. From these studies, it is clear that the helical region of PEX14 (amino acids 138-200; shown in blue) binds to the helix of OPTN (amino acids 420-510), while other regions exhibit a slightly looser interaction (Extended Data Figs. 6a (left image) and 7a,b). To complement the AF2 predictions, we conducted a 50 ns molecular dynamics simulation and selected the conformation at the lowest energy point (Extended Data Fig. 7c), as depicted in Extended Data Fig. 6a (right image). The binding between the proteins became tighter. The helical region of PEX14 showed bending and tended to embrace the OPTN protein. Furthermore, no separation was observed between the proteins throughout the molecular dynamics simulation process, indicating stable binding between them. Overall, the molecular dynamics effectively illustrated the molecular mechanism of close interaction between the proteins. As depicted in Extended Data Fig. 6b, the average root mean square deviation (RMSD) of the protein complex is 1.28±0.18 Å, and the system reached dynamic equilibrium at around 10 ns, indicating that the interactions between the proteins rapidly stabilized during the molecular dynamics process. In addition, we observed no significant discontinuities in the conformational changes of the complex, affirming the robust binding among the three proteins and solidifying the overall stability of the complex. The root mean square fluctuation (RMSF) plots (Extended Data Figure 7d) indicate that only a small number of amino acids in the protein complex undergo significant conformational changes, particularly around residue 100 of PEX14. This can likely be attributed to the location of these amino acids in the hinge region of the protein, which inherently exhibits greater flexibility. In addition, we analyzed the variation in the number of hydrogen bonds between the proteins throughout the simulation process. According to the hydrogen bond network diagram (Extended Data Figure 7e), it is evident that multiple hydrogen bond interactions can form between the proteins. For example, an average of 10.29 ± 1.98 hydrogen bonds form between the two OPTN modules, 11.90 ± 4.2 hydrogen bonds between OPTN (A) and PEX14,

and 11.45 ± 3.43 hydrogen bonds between OPTN (B) and PEX14. The similar number of hydrogen bonds indicates that the complex formed by the three proteins is tightly bound, exhibiting a pronounced aggregative effect and providing support for the stability of the protein-protein interactions. Last but not least, according to the radius of gyration (Rg) plot (Extended Data Fig. 7f), we observed a significant decrease in the Rg of the complex protein during the simulation. This decrease is likely a result of the binding between proteins, which promotes more hydrophobic contacts and effective internal interactions, leading to a better fit and enhanced stability of the complex. This finding is consistent with a solvent-accessible surface area (SASA) (Extended Data Fig. 7g), which shows a significant decrease, indicating the presence of strong hydrophobic interactions between the proteins. Combined with the binding-free energy calculation (Extended Data Table 1), we can conclude that hydrophobic interactions and van der Waals forces make a significant contribution to the stability of complexes, followed by electrostatic interactions. The binding free energy between the two OPTN fragments is notably low (-257.14 ± 7.91 kcal/mol), with van der Waals forces contributing substantially (-224.88 ± 5.9 kcal/mol) and electrostatic interactions also playing a significant role (-41.54 ± 4.1 kcal/mol), primarily due to the formation of effective hydrogen bonds between the proteins. Similarly, OPTN (A, B) and PEX14 (C) display strong affinity interactions, with binding free energies of -129.95 ± 10.69 kcal/mol and -229.54 ± 10.54 kcal/mol, respectively. Notably, the affinity between OPTN proteins is stronger, facilitating easier dimer formation. However, PEX14 also shows a strong affinity for the OPTN dimer. Combined with the modeling after simulation (Extended Data Fig. 6 and Extended Data Movie 1), this suggests that PEX14 may wrap around the OPTN dimer, resulting in stable trimeric complexes.

## Discussion

In this study, we identified PEX14 as a key factor in OPTN-mediated pexophagy in HEK-293 cells. Surprisingly, our domain mapping studies revealed that ectopic expression of OPTN variants lacking functional ATG9A- and LC3-binding motifs, necessary for its autophagic function, could still induce pexophagy (Fig. 3). However, the induction of pexophagy depended on the presence of the UBD (Fig. 4a,b), a domain renowned for its affinity towards linear ubiquitin chains [40], and for its crucial role in facilitating the assembly of homotrimers [38]. Notably, $OPTN_{\Delta 474-479}$, a protein unable to bind polyubiquitin chains [41], was capable of initiating pexophagy (Fig. 4e,f), and the downregulation of endogenous OPTN interfered with $OPTN_{217-577}$-GFP-induced pexophagy (Fig. 5). This suggests that pexophagy induction by the latter protein occurs through oligomerization with endogenous OPTN, a finding supported by AF2 predictions and MD simulations (Extended Figs. 6 and 7, Extended Table 1). Furthermore, our GFP-Trap pull-down experiments unveiled the intriguing finding that the UBD domain of OPTN, even in the absence of ubiquitin-binding activity, oligomerizes with the coiled-coil domain of PEX14 (Figs. 4a-d and 6a,b). Prior studies have already established the involvement of this domain in PEX14 homo-oligomerization [39,42].

Pexophagy involves a range of receptors (e.g., NBR1, SQSTM1, and OPTN), but their interplay remains poorly understood. Our findings demonstrate that OPTN-mediated pexophagy is specific to certain cell types (Fig. 1), prompting questions about the factors and signaling mechanisms governing this specificity. One compelling hypothesis involves cell type-specific posttranslational modifications. This idea finds support in the recognition that phosphorylation, ubiquitylation, and acetylation are acknowledged for their involvement in initiating, regulating, and fine-tuning autophagy [43]. In addition, both OPTN and PEX14 can undergo phosphorylation at multiple sites (see PTM sections in UniProt Q96CV9 and O75381, respectively). Notably, the phosphorylation of OPTN by TBK1 (e.g., at S177 and S473) [44], a top-ranked proximity partner of OPTN in our BioID experiments (Fig. 2B), has been linked to selective autophagy of cytosolic bacteria [37], mutant protein aggregates [26], and damaged mitochondria [44]. Note that, even though the ectopic expression of $OPTN_{217-577}$-GFP and $OPTN_{\Delta 474-479}$-GFP induces pexophagy, the question remains whether TBK1-mediated phosphorylation of OPTN at S177 and S473 is also essential for the effective promotion of pexophagy. This consideration arises due to the potential oligomerization of

these proteins with endogenous OPTN. Another hypothesis suggests the involvement of a yet-to-be-identified protein that either recruits OPTN to or activates it at the peroxisomal membrane in a cell type-specific manner. However, uncovering the identity and precise function of such a protein awaits further investigation.

Another intriguing question yet to be addressed is the role of OPTN-mediated pexophagy in both health and disease. In this context, it is worth noting that, until now, the role of OPTN in pexophagy research has largely been overlooked, with most attention directed towards the autophagy receptors SQSTM1 and NBR1. However, the recent observations that (i) pexophagy is increased in two autosomal dominant Zellweger spectrum disorder patients with C-terminally truncated PEX14 variants (p.A196Lfs∗34 and p.A196Vfs∗34), and (ii) this increase in pexophagy can only be partially mitigated by NBR1 knockdown [45], indirectly suggests that the dominant phenotype may also be partially caused by a dysregulated PEX14-OPTN pexophagy axis. In addition, considering that (i) an increase in pro-inflammatory cytokines correlates with heightened expression levels of OPTN [46,47], and (ii) prolonged fasting induces the production of such cytokines and selective pexophagy in the liver of catalase-deficient mice [48], it is reasonable to suggest that a physiological upregulation of OPTN may suffice to elicit pexophagy in a manner tailored to tissue demands, energetics, and metabolic needs.

In summary, the findings of this study represent a crucial initial step in unraveling OPTN-mediated pexophagy, a process that apparently resembles the ubiquitin-independent function of OPTN in aggrephagy [26]. Continued investigation into the molecular mechanisms behind OPTN-mediated pexophagy offers the potential to deepen our understanding of disorders associated with peroxisome dysfunction and OPTN malfunction. Moreover, such research endeavors may catalyze the development of innovative interventions targeting these conditions.

## Methods

### DNA manipulations and plasmids

The mammalian expression plasmids encoding mCherry-PTS1 (pMF1218) [49], po-mKeima (pMF2005) [25], non-tagged HsPEX14 [50], HsPEX14-GFP (pMF120) [51], or $GFP_{Nb}$-PM (pMF1968) [52] have been described elsewhere. The flippase (Flp) recombinase expression vector (pOG44; Thermo Fisher Scientific, V600520), the Flp-InTM inducible expression vector (pcDNA5/FRT/TO; Thermo Fisher Scientific, V652020), the lentiviral GFP expression vector (pLenti CMV GFP Puro; Addgene, plasmid 17448), and the plasmids encoding GFP (Clontech, 6085-1), the pOPINE GFP nanobody (Addgene, plasmid 49172 [53]), non-tagged $OPTN_{1-577}$ (Origene, SC319257), $OPTN_{1-577}$-GFP (Addgene, plasmid 27052 [54]), $OPTN_{1-209}$-GFP (Addgene, plasmid #68839 [41]), $OPTN_{217-577}$-GFP (Addgene, plasmid #68841 [41]), or $OPTN_{D474N}$-GFP (Addgene, plasmid #68847 [41]) were commercially obtained. The miniTurbo BirA template was kindly provided by Dr. P. Kim (University of Toronto, Canada). All newly generated plasmids, as well as the primers (Integrated DNA Technologies) used to produce these plasmids, have been described in Supplementary Tables 2 and 1, respectively. The *TOP10F' E. coli* strain (Thermo Fisher Scientific, C3030-06) was routinely used as a cloning and plasmid amplification host. However, upon using the NEBuilder® HiFi DNA Assembly Master Mix (New England Biolabs, M5520AVIAL) or the Q5 Site-Directed Mutagenesis Kit (New England Biolabs, E0554), the DpnI (Thermo Fisher Scientific, ER1707)-treated mixtures, free of parental plasmid, were transformed in DH5α cells (Thermo Fisher Scientific, 18265017). All plasmids were validated by DNA sequencing (LGC Genomics, Germany).

### Cell lines and culture conditions

The following cell lines were used for this study: human embryonic kidney cells (HEK-293, ECACC 85120602), Flp-in T-REx 293 cells (Thermo Fisher Scientific, R78007), lenti-GFP Flp-In T-REx 293 cells (this study), lenti-$OPTN_{1-577}$-GFP Flp-In T-REx 293 cells (this study), GFP Flp-In T-REx 293 cells (this study), $OPTN_{1-577}$-GFP Flp-In T-REx 293 cells (this study), lenti-po-mKeima Flp-In-T-REx 293 cells [25], human cervical cancer cells (HeLa, ECACC 93021013), po-mKeima HeLa cells [25], human colorectal carcinoma cells (HCT116, ECACC 91091005), po-mKeima HCT116 (this study), and Chinese hamster ovary cells (CHO, ECACC 85050302). The novel Flp-In T-REx 293, lenti-Flp-In T-REx 293, and po-mKeima-expressing cell lines were

generated as detailed elsewhere [25,55-57]. HEK-293, Flp-in T-REx 293, and HeLa cells were cultured in DMEM medium (Gibco, 31966-047) supplemented with 10% (v/v) fetal bovine serum (FBS; Biowest, S181B) and 0.2% (v/v) MycoZap (Lonza, VZA-2012) in a humidified atmosphere of 5% $CO_2$ at 37°C. HCT116 and CHO cells were cultured similarly, using DMEM/F12 medium (Gibco, 21041-033) and the same supplements plus 2 mM UltraGlutamine I (Lonza, BE17-605E/U1).

**Cell transfection and treatment procedures**

Flp-In T-REx 293 cells were either electroporated with the Neon Transfection system (Thermo Fisher Scientific) [25] for fluorescence microscopy imaging and flow cytometry analyses or transfected using the JetPrime reagent (Polyplus, 114-01) for IP experiments. HCT116 and HeLa cells were transfected with the Lipofectamine 3000 reagent (Invitrogen, L3000015), and CHO cells were transfected with polyethyleneimine [58]. To prevent autophagosome-lysosome fusion, the cells were pretreated for 2 h with 200 nM bafilomycin A1 (BafA1; Cayman Chemical, 11038). The same volume of DMSO (MP Biomedicals, 02196055) was included as vehicle control. To image mitochondria, the endoplasmic reticulum, and lysosomes, the cells were incubated with MitoTracker™ Red CM-H2Xros (Thermo Fisher Scientific, M7513; 1:2000), ER-Tracker™ Blue-White DPX (Thermo Fisher Scientific, E12353; 1:2000), and LysoTracker™ Red DND-99 (Thermo Fisher Scientific, L7528; 1:5000), respectively. To downregulate OPTN expression, the cells underwent transfection (using Lipofectamine 3000) twice with the OPTN DsiRNA hs.Ri.OPTN.13.10 (sense strand: 5’-aagcuaaauaaucaagc-3’; antisense strand: 5'-cuuucauggcuugauuau-3’; final concentration: 50 nM), with a 48-h interval between each transfection. A non-targeting DsiRNA (Integrated DNA Technologies, 51-01-14-03), which does not recognize any human sequences, was used as a control.

**Antibodies and streptavidin conjugates**

The following primary antibodies were used for immunofluorescence (IF) or immunoblotting (IB): rabbit anti-OPTN (Abcam, ab23666; IF, 1:50; IB, 1:1000), mouse anti-GAPDH (Sigma-Aldrich, G8795; IB, 1:2000), rabbit anti-GFP (IB, 1:50000) [59], rabbit anti-PEX14 (IB, 1:1000) [60], and mouse anti-PEX14 (IF, 1:1000) [61]. The secondary antibodies for IF were conjugated to Alexa Fluor 488 (Invitrogen, A11017; 1:2000) or Texas Red (Calbiochem,

Darmstadt, Germany; 401355; 1:200). Streptavidin-horseradish peroxidase (IB, 1:3000) was from Sigma-Aldrich (RABHRP3).

**Immunoblotting and densitometric analysis**

Antigen-antibody and biotin-streptavidin complexes were detected by using the Amersham ECL Western Blotting Detection Reagent (Cytiva, RPN2235) in combination with the ImageQuant LAS4000 system (GE Healthcare). Images were further processed and quantified with AlphaView Software (ProteinSample) or ImageJ software [62].

**Fluorescence microscopy**

Fluorescence microscopy was conducted as previously described [63]. For live-cell imaging, the cells were seeded and imaged in FluoroDish cell culture dishes (World Precision Instruments, FD35), either pre-coated with 25 µg/mL polyethyleneimine (MP Biomedicals, 195444) for HEK-293 cells or left uncoated for other cell types. For immunofluorescence microscopy, cells were seeded onto (polyethyleneimine-coated) glass coverslips, and subsequently fixed and processed following methods outlined elsewhere [64]. Image acquisition and analysis were performed using the cellSens Dimension software (version 2.1) (Olympus Belgium). Nanobody-based plasma membrane translocation assays were executed following established procedures [52].

**Structured illumination microscopy**

Cells were cultured and imaged in Fluorodishes (World Precision Instruments, FD35). For image acquisition, a Nikon Ti2 N-structured illumination (SIM) S microscope (Nikon Instruments) equipped with an ORCA-Flash4.0 sCMOS camera (Hamamatsu, C13440) and a Nikon SR Apo TIRF 100x objective lens (NA 1.49) was controlled by Nikon NIS-Elements imaging software (version 5.21.03). Multicolored images were acquired in three-dimensional SIM mode (with three angles and five phases) with a Z-stack (0.100 µm step size) at room temperature. The fluorescence of GFP, excited at 488 nm, was captured using a 525/30 bandpass filter, and the fluorescence of mCherry, excited at 561 nm, was detected with a 595/30 bandpass filter. The images were reconstructed and analyzed using Arivis Vision4D (version 3.3) and Nikon NIS-Elements AR 5.40 software.

**Flow cytometry analysis**

The po-mKeima-expressing cells were washed with DPBS and dislodged from the plate by trypsinization. Next, the cells were pelleted (300× g, 1 min), resuspended in culture medium, and analyzed through FACSymphony™ A1 flow cytometry (BD Biosciences) by using 405- and 561-nm lasers in combination with a 600–620 nm emission filter (for mKeima), and a 488-nm laser with a 505-560 nm emission filter (for GFP); For each sample, 100,000 events were collected and analyzed using BD FACSDiva v8.0.1 software (BD Biosciences).

**MiniTurbo proximity labeling, affinity purification, and sample preparation for LC-MS analysis**

Cells were seeded in 15-cm dishes and transfected with 6 µg of a plasmid encoding miniTurbo-OPTN-GFP (pHL30). After 48 h, the cells were pretreated with 200 nM of BafA1 for 2 h and subsequently incubated with or without 50 µM D-biotin (Sigma-Aldrich, B4501) for 30 min. Next, the cells were rinsed with ice-cold PBS (Lonza, BE17-512F) and lysed on ice for 20 min using lysis buffer (50 mM Tris-HCl (pH 7.5), 150 mM NaCl, 1% (w/v) Triton X-100, 1 mM EDTA) supplemented with protease (Sigma-Aldrich, P2714) and phosphatase (Sigma-Aldrich, P5726) inhibitor cocktails. Subsequently, the lysates were sonicated (Diagnode Bioruptor UCD-200) in three 10-s cycles at high intensity and then cleared by centrifugation at 10,000 × g for 10 min. A small portion of the supernatant was taken for biotin IB validation, and the remaining supernatant was further incubated with 25 µL of Streptavidin Sepharose beads (Cytiva, 90100484) overnight at 4°C. After discarding the supernatant, the beads were washed 3 times with 200 µL of lysis buffer and 3 times with 200 µL of ammonium bicarbonate (50 mM, pH 7.8). Thereafter, the beads were resuspended in 200 µL of ammonium bicarbonate solution, and 250 ng of mass spectrometry grade trypsin (Promega, V528A) was added. The samples were digested for 14 hours at 37°C in an Eppendorf Thermomixer C (speed: 750 rpm), and a 2-µL sample was taken for tryptic digestion quality control using a Dionex™ UltiMate™ 3000 RSLC Nano System (Thermo Fisher Scientific). The reduction and carbamidomethylation of disulfide bridges in the supernatant were performed by treating the samples with 10 mM dithiothreitol (VWR, M109) for 30 minutes at 56°C, followed by the addition of 30 mM iodoacetamide (Sigma-Aldrich, I1149) for an additional 30 minutes at room temperature. Next, the carbamidomethylated samples were acidified using 10% trifluoroacetic acid (Biosolve, 202341) and subsequently subjected to desalting using Poros Oligo R3 reversed-phase resin (Thermo Fisher Scientific, 1133903).

The bound peptides were washed twice with 0.1% formic acid (FA; Thermo Fisher Scientific, 28905) in water and eluted with 100 µL of 60% (v/v) acetonitrile (ACN; Sigma, 34851) in water containing 0.1% FA. Finally, the eluates were dried under vacuum, and the peptides were resolubilized in 10 µL of 0.1% FA.

**LC-MS analysis**

Digested samples (10% of total volume) were injected into an UltiMate 3000 RSLC nano System (Dionex) coupled to an Orbitrap Lumos Tribrid Mass Spectrometer (Thermo Fisher Scientific). After initial loading, peptides were concentrated on a 75 µm × 2 cm C18 pre-column using 0.1% (v/v) trifluoroacetic acid at a flow rate of 20 µL/min. Sample separation was accomplished on a reversed-phase column (Acclaim C18 PepMap100; pore size: 75 µm; length: 50 cm) at 60°C using a binary gradient (A: 0.1% FA; B: 84% ACN with 0.1% FA) at a flow rate of 250 nL/min: 3% solvent B for 5 min, a linear increase of solvent B to 32% for 95 min followed by washing with 95% solvent B for 3 min and a linear decrease of solvent B to 3% for 1 min. Peptides were ionized by using a nanospray ESI source. MS survey scans were acquired on the Orbitrap Lumos Tribrid by using the following settings: mass spectrometer was operated in data-dependent acquisition mode (DDA) with full MS scans from 350 to 1500 m/z at a resolution of 120,000 at 200 m/z (Orbitrap) using the polysiloxane ion at 445.12002 m/z as lock mass. The automatic gain control (AGC) was set to 4E5, the maximum injection time to 100 ms, and the RF amplitude to 40%. The top intense ions (ion intensity ≥ 5E3, charge state = 2-7) were selected within a 1.2 m/z mass isolation window for fragmentation at a normalized collision energy of 32% in each cycle 3 seconds of the acquisition analysis, following each survey scan. The dynamic exclusion time was set to 60 s. Fragment ions were acquired in the ion trap.

**Data analysis of miniTurbo proximity labeling**

Raw data were searched against the UniProt human database (June 2023; 20,409 target sequences, including OPTN-GFP) using Sequest HT on Proteome Discoverer v2.5. Precursor mass tolerance was limited to 20 ppm and fragment mass tolerance to 0.5 Da. Cleavage specificity was set to fully tryptic, allowing for a maximum of two missed cleavages. Carbamidomethylation of cysteines (+57.0214 Da) was defined as a fixed modification and oxidation of methionine (+15.9949 Da) as a variable modification for all searches. The results were evaluated with Percolator for false discovery rate (FDR) estimation and data were

filtered at ≤1% FDR on the PSM and peptide level and filtered ‘master’ proteins at protein level [65]. Unique peptides (except modified peptides) were taken for Label free quantification (LFQ). Next, the sum of top three peptide intensities was calculated to determine the protein intensities. Protein intensities were normalized to total peptide amount. P-values between the sample groups (four biological replicates, with or without D-biotin treatment) were determined by a two-sided t-test with false discovery rate (FDR) correction. Common contaminating proteins were removed from the hit lists. The significance cut-offs employed were unique peptides ≥ 2, adjust p-value ≤ 0.05 and $\log_2$(ratio biotin/no biotin) ≥ 1. LFQ Data was plotted and visualized by GraphPad Prism 9.0.0. The raw data of LC-MS runs are available via ProteomeXchange with identifier PXD037891.

**Immunoprecipitation using GFP-Trap**

HEK-293 cells were cultured in 10-cm cell culture dishes and transfected with 6 µg of plasmid. Two days later, the cells were cultured for 2 h in the presence of 200 nM BafA1. After rinsing with ice-cold PBS, cleared supernatant fractions were prepared similarly to the miniTurbo proximity labeling samples and subjected to a GFP-Trap assay [66]. Briefly, the supernatants were divided into two portions for input detection and GFP-Trap. The input fractions were supplemented with 3x SDS-PAGE sample buffer for IB analysis and boiled at 100 °C for 10 min. The supernatants for GFP-Trap immunoprecipitation were pre-cleared with 30 µL of homemade BSA beads for 30 min at 4 °C, followed by incubation with 25 µL of homemade GFP-Trap beads for 2 h at 4 °C (the BSA- and pOpine-GFP nanobody-conjugated beads were prepared as described elsewhere [67]). Next, the beads were washed 6-8 times with high saline lysis buffer (150 mM Tris-HCl (pH 7.5), 500 mM NaCl, 1% (w/v) Triton X-100, 1 mM EDTA), boiled in 3x SDS-PAGE sample buffer, and after a quick spin, the supernatants were subjected to IB [25].

**AlphaFold-multimer modeling and molecular dynamics simulation**

The AlphaFold structural prediction was performed as previously described [68], and the following sequences were submitted: human $OPTN_{420-510}$ (protein A; reference sequence: UniProt Q96CV9-1), human $OPTN_{420-510}$ (protein B; reference sequence: UniProt Q96CV9-1), and human $PEX14_{1-200}$ (protein C; reference sequence: UniProt O75381-1). The modes were processed and visualized in (pyMOL, Version 2.0; Schrodinger LLC, USA). To further explore the stability and affinity of the OPTN-OPTN-PEX14 complex and obtain the optimal complex

conformation, we conducted a 50 ns molecular dynamics (MD) simulation. All MD simulations for complex systems were performed using the GROMACS (gmx) 2020.1 package with the AMBER99SB-ILDN force field. The initial protein structures were solvated in a dodecahedron box using the transferable intermolecular potential 3-point water model. The simulation boxes were constructed with a margin of at least 12 Å between the OPTN-OPTN-PEX14 complex and the periodic box boundaries. The simulation systems were neutralized by adding a concentration of 0.15 M of NaCl (physiological condition). Long-range electrostatics interactions were modeled using the Particle mesh Ewald algorithm, with a direct space cut-off distance set to 12 Å. The van der Waals interactions were calculated using a force-switched cut-off between 10 and 12 Å. The linear constraint solver algorithm was applied to constrain hydrogen bonds, with an integration time step of 2.0 fs. The steepest descent algorithm was applied to minimize the system for 5,000 steps. Subsequently, equilibration under the NVT ensemble at 300 K was conducted for 500 ps. The NPT equilibration was then applied at 1 bar pressure and 300 K temperature for 500 ps, ensuring a balance of the solvent molecules around protein residues. The temperature coupling, with a time constant of 0.1 ps, was done using the velocity rescaling algorithm, and the pressure was controlled using the Parrinello-Rahman barostat algorithm, with a time constant of 5 ps. The well-equilibrated system underwent MD simulations for 50 ns each at 300 K without any constraints. Following this, we utilized the gmx trjconv module to analyze molecular dynamics trajectories and obtain structural and dynamic properties, such as root mean square deviation (RMSD), root mean square fluctuation (RMSF), radius of gyration, solvent accessible surface area (SASA), hydrogen bond interactions, principal component analysis (PCA), free energy landscape (FEL), and the total energy of the system. In addition, the binding free energy between proteins was calculated using the gmx Molecular Mechanics Poisson-Boltzmann Surface Area (MMPBSA) approach.

**Statistical analysis**

Statistical analysis involved conducting one-way analysis variance (ANOVA) followed by Tukey's post hoc test for multiple comparisons. Student's unpaired two-tailed t-test was used to compare two groups. All statistical analyses were conducted using GraphPad Prism (version 9.0.0 for Windows 64-bit, GraphPad Software, San Diego, CA, USA). Results with a p-value less than 0.05 were considered statistically significant.

**Varia**

The data used to generate Fig. 2b, the schematic depicting the distinct domains and major interactions of OPTN, were gathered from multiple sources [69-72].

## Author contributions

H.L. and M.F. conceptualized the study and designed the experiments. H.L, S.C., and S.V. conducted the proteomics analyses. Y.L. generated the lentivirus particles and the stable lentiviral cell lines. D.I. and W.V generated the plasmids encoding $OPTN_{\Delta 474-479}$ and $OPTN_{\Delta 545-577}$. Z.C. and B.V. assisted in the GFP-Trap assay and AlphaFold modeling. H.L., S.C., and Z.C. performed the other experiments. H.L, C.L., C.C., M.A.H., M.B., and M.F. analyzed and interpreted the data. C.L. and M.F. coordinated and supervised the project. M.F. and M.B. provided resources and funding for the investigation. H.L. and M.F. wrote the original draft of the manucript, and all authors edited the draft and agreed on the content of the submitted version of the manuscript.

## Acknowledgments

The authors acknowledge the following entities and individuas for their invaluable support: the VIB Bio Imaging and FACS Core facilities (KU Leuven) for assisting in super-resolution imaging and FACS analysis, the John Creemers lab (KU Leuven) for lentiviral packaging, Dr. C.F Wu for guiding AlphaFold-multimer modeling and molecular dynamics simulations, Dr. M. Bollen (KU Leuven, Belgium) for providing the HCT116 cell line, Ms. S. Lemaire and Mr. X.Y Cao (KU Leuven, Belgium) for valuable advice regarding the GFP-Trap assay, Dr. R.J. Wanders (University of Amsterdam, The Netherlands) for the plasmid encoding non-tagged HsPEX14, Dr. P. Kim (University of Toronto, Canada) for the miniTurbo BirA template, and Dr. B. Yue (University of Illinois, Chicago, IL, USA) for the plasmids encoding $OPTN_{1-577}$-GFP, $OPTN_{1-209}$-GFP, $OPTN_{211-577}$-GFP, or $OPTN_{D474N}$-GFP. This work received support from H2020-MSCA-ITN (812968) PERICO, the Research Foundation-Flanders (G091819N,1213623N), the China Scholarship Council (201906790005), KU Leuven (C14/18/088), and the Ministry of Higher Education of the Arab Republic of Egypt.

## References


1. Klionsky DJ, Petroni G, Amaravadi RK et al. Autophagy in major human diseases. EMBO J 2021, 40:e108863. https://dx.doi.org/10.15252/embj.2021108863

2. Rahman MA, Ahmed KR, Haque F, Park MN, Kim B. Recent advances in cellular signaling interplay between redox metabolism and autophagy modulation in cancer: an overview of molecular mechanisms and therapeutic interventions. Antioxidants 2023, 12:428. https://dx.doi.org/10.3390/antiox12020428

3. Wanders RJA, Baes M, Ribeiro D, Ferdinandusse S, Waterham HR. The physiological functions of human peroxisomes. Physiol Rev 2023, 103:957-1024. https://dx.doi.org/10.1152/physrev.00051.2021

4. Li H, Lismont C, Revenco I, Hussein MAF, Costa CF, Fransen M. The peroxisome-autophagy redox connection: a double-edged sword? Front Cell Dev Biol 2021, 9:814047. https://dx.doi.org/10.3389/fcell.2021.814047

5. Bajdzienko J, Bremm A. Mammalian pexophagy at a glance. J Cell Sci 2024, 137:jcs259775. https://dx.doi.org/10.1242/jcs.259775

6. Deosaran E, Larsen KB, Hua R, Sargent G, Wang Y, Kim S, Lamark T, Jauregui M, Law K, Lippincott-Schwartz J, Brech A, Johansen T, Kim PK. NBR1 acts as an autophagy receptor for peroxisomes. J Cell Sci 2013, 126:939-952. https://dx.doi.org/10.1242/jcs.114819

7. Yamashita S, Abe K, Tatemichi Y, Fujiki Y. The membrane peroxin PEX3 induces peroxisome-ubiquitination-linked pexophagy. Autophagy 2014, 10:1549-1564. https://dx.doi.org/10.4161/auto.29329

8. Zhang J, Tripathi DN, Jing J, Alexander A, Kim J, Powell RT, Dere R, Tait-Mulder J, Lee JH, Paull TT, Pandita RK, Charaka VK, Pandita TK, Kastan MB, Walker CL. ATM functions at the peroxisome to induce pexophagy in response to ROS. Nat Cell Biol 2015, 17:1259-1269. https://dx.doi.org/10.1038/ncb3230

9. Riccio V, Demers N, Hua R, Vissa M, Cheng DT, Strilchuk AW, Wang Y, McQuibban GA, Kim PK. Deubiquitinating enzyme USP30 maintains basal peroxisome abundance by regulating pexophagy. J Cell Biol 2019, 218:798-807. https://dx.doi.org/10.1083/jcb.201804172

10. Nordgren M, Francisco T, Lismont C, Hennebel L, Brees C, Wang B, Van Veldhoven PP, Azevedo JE, Fransen M. Export-deficient monoubiquitinated PEX5 triggers peroxisome removal in SV40 large T antigen-transformed mouse embryonic fibroblasts. Autophagy 2015, 11:1326-1340. https://dx.doi.org/10.1080/15548627.2015.1061846

11. Sargent G, van Zutphen T, Shatseva T, Zhang L, Di Giovanni V, Bandsma R, Kim PK. PEX2 is the E3 ubiquitin ligase required for pexophagy during starvation. J Cell Biol 2016, 214:677-690. https://dx.doi.org/10.1083/jcb.201511034

12. Gubas A, Dikic I. A guide to the regulation of selective autophagy receptors. FEBS J 2022, 289:75-89. https://dx.doi.org/10.1111/febs.15824

13. Hara-Kuge S, Fujiki Y. The peroxin Pex14p is involved in LC3-dependent degradation of mammalian peroxisomes. Exp Cell Res 2008, 314:3531-3541. https://dx.doi.org/10.1016/j.yexcr.2008.09.015

14. Jiang L, Hara-Kuge S, Yamashita S, Fujiki Y. Peroxin Pex14p is the key component for coordinated autophagic degradation of mammalian peroxisomes by direct binding to LC3-II. Genes Cells 2015, 20:36-49. https://dx.doi.org/10.1111/gtc.12198

15. Fransen M, Terlecky SR, Subramani S. Identification of a human PTS1 receptor docking protein directly required for peroxisomal protein import. Proc Natl Acad Sci USA 1998, 95:8087-8092. https://dx.doi.org/1010.1073/pnas.95.14.8087

16. Maeda S, Yamamoto H, Kinch LN, Garza CM, Takahashi S, Otomo C, Grishin NV, Forli S, Mizushima N, Otomo T. Structure, lipid scrambling activity and role in autophagosome formation of ATG9A. Nat Struct Mol Biol 2020, 27:1194-1201. https://dx.doi.org/10.1038/s41594-020-00520-2

17. Li X, Han H, Zhou MT, Yang B, Ta AP, Li N, Chen J, Wang W. Proteomic analysis of the human tankyrase protein interaction network reveals its role in pexophagy. Cell Rep 2017, 20:737-749. https://dx.doi.org/10.1016/j.celrep.2017.06.077

18. Chen BH, Chang YJ, Lin S, Yang WY. Hsc70/Stub1 promotes the removal of individual oxidatively stressed peroxisomes. Nat Commun 2020, 11:5267. https://dx.doi.org/10.1038/s41467-020-18942-3.

19. Wilhelm LP, Zapata-Muñoz J, Villarejo-Zori B, Pellegrin S, Freire CM, Toye AM, Boya P, Ganley IG. BNIP3L/NIX regulates both mitophagy and pexophagy. EMBO J 2022, 41:e111115. https://dx.doi.org/10.15252/embj.2022111115

20. Barone FG, Urbé S, Clague MJ. Segregation of pathways leading to pexophagy. Life Sci Alliance 2023, 6:e202201825. https://dx.doi.org/10.26508/lsa.202201825

21. Nazarko TY. Pexophagy is responsible for 65% of cases of peroxisome biogenesis disorders. Autophagy 2017, 13:991-994. https://dx.doi.org/10.1080/15548627.2017.1291480

22. Cho DH, Kim YS, Jo DS, Choe SK, Jo EK. Pexophagy: molecular mechanisms and implications for health and diseases. Mol Cells 2018, 41:55-64. https://dx.doi.org/10.14348/molcells.2018.2245

23. Germain K, So RWL, DiGiovanni LF, Watts JC, Bandsma RHJ, Kim PK. Upregulated pexophagy limits the capacity of selective autophagy. Nat Commun 2024, 15:375. https://dx.doi.org/10.1038/s41467-023-44005-4

24. Qiu Y, Wang J, Li H, Yang B, Wang J, He Q, Weng Q. Emerging views of OPTN (optineurin) function in the autophagic process associated with disease. Autophagy 2022, 18:73-85. https://dx.doi.org/10.1080/15548627.2021.1908722

25. Li H, Lismont C, Costa CF, Hussein MAF, Baes M, Fransen M. Enhanced levels of peroxisome-derived $H_2O_2$ do not induce pexophagy but impair autophagic flux in HEK-293 and HeLa cells. Antioxidants 2023, 12:613. https://dx.doi.org/10.3390/antiox12030613

26. Korac J, Schaeffer V, Kovacevic I, Clement AM, Jungblut B, Behl C, Terzic J, Dikic I. Ubiquitin-independent function of optineurin in autophagic clearance of protein aggregates. J Cell Sci 2013, 126:580-592. https://dx.doi.org/10.1242/jcs.114926

27. Nguyen TN, Sawa-Makarska J, Khuu G, Lam WK, Adriaenssens E, Fracchiolla D, Shoebridge S, Bernklau D, Padman BS, Skulsuppaisarn M, Lindblom RSJ, Martens S, Lazarou M. Unconventional initiation of PINK1/Parkin mitophagy by optineurin. Mol Cell 2023, 83:1693-1709.e9. https://dx.doi.org/10.1016/j.molcel.2023.04.021

28. Yamano K, Sawada M, Kikuchi R, Nagataki K, Kojima W, Endo R, Kinefuchi H, Sugihara A, Fujino T, Watanabe A, Tanaka K, Hayashi G, Murakami H, Matsuda N. Optineurin provides a mitophagy contact site for TBK1 activation. EMBO J 2024, 43:754-779. https://dx.doi.org/10.1038/s44318-024-00036-1

29. Padman BS, Nguyen TN, Uoselis L, Skulsuppaisarn M, Nguyen LK, Lazarou M. LC3/GABARAPs drive ubiquitin-independent recruitment of optineurin and NDP52 to amplify mitophagy. Nat Commun 2019, 10:408. https://dx.doi.org/10.1038/s41467-019-08335-6

30. Yamano K, Kikuchi R, Kojima W, Hayashida R, Koyano F, Kawawaki J, Shoda T, Demizu Y, Naito M, Tanaka K, Matsuda N. Critical role of mitochondrial ubiquitination and the OPTN-ATG9A axis in mitophagy. J Cell Biol 2020, 219:e201912144. https://dx.doi.org/10.1083/jcb.201912144

31. Qin W, Cho KF, Cavanagh PE, Ting AY. Deciphering molecular interactions by proximity labeling. Nat Methods 2021, 18:133-143. https://dx.doi.org/10.1038/s41592-020-01010-5

32. Morton S, Hesson L, Peggie M, Cohen P. Enhanced binding of TBK1 by an optineurin mutant that causes a familial form of primary open angle glaucoma. FEBS Lett 2008, 582:997-1002. https://dx.doi.org/10.1016/j.febslet.2008.02.047

33. Nazarko TY, Ozeki K, Till A, Ramakrishnan G, Lotfi P, Yan M, Subramani S. Peroxisomal Atg37 binds Atg30 or palmitoyl-CoA to regulate phagophore formation during pexophagy. J Cell Biol 2014, 204:541-557. https://dx.doi.org/10.1083/jcb.201307050

34. Law KB, Bronte-Tinkew D, Di Pietro E, Snowden A, Jones RO, Moser A, Brumell JH, Braverman N, Kim PK. The peroxisomal AAA ATPase complex prevents pexophagy and development of peroxisome biogenesis disorders. Autophagy 2017, 13:868-884. https://dx.doi.org/10.1080/15548627.2017.1291470

35. Park NY, Jo DS, Park SJ, Lee H, Bae JE, Hong Y, Kim JB, Kim YH, Park HJ, Choi JY, Lee HJ, Ryoo ZY, Lee HS, Kim JC, Lee EK, Cho DH. Depletion of HNRNPA1 induces peroxisomal autophagy by regulating PEX1 expression. Biochem Biophys Res Commun 2021, 545:69-74. https://dx.doi.org/10.1016/j.bbrc.2021.01.083

36. Gleason CE, Ordureau A, Gourlay R, Arthur JSC, Cohen P. Polyubiquitin binding to optineurin is required for optimal activation of TANK-binding kinase 1 and production of interferon β. J Biol Chem 2011, 286:35663-35674. https://dx.doi.org/10.1074/jbc.M111.267567

37. Wild P, Farhan H, McEwan DG, Wagner S, Rogov VV, Brady NR, Richter B, Korac J, Waidmann O, Choudhary C, Dötsch V, Bumann D, Dikic I. Phosphorylation of the autophagy receptor optineurin restricts Salmonella growth. Science 2011, 333:228-233. https://dx.doi.org/10.1126/science.1205405

38. Gao J, Ohtsubo M, Hotta Y, Minoshima S. Oligomerization of optineurin and its oxidative stress- or E50K mutation-driven covalent cross-linking: possible relationship with glaucoma pathology. PLoS One 2014, 9:e101206. https://dx.doi.org/10.1371/journal.pone.0101206

39. Fransen M, Brees C, Ghys K, Amery L, Mannaerts GP, Ladant D, Van Veldhoven PP. Analysis of mammalian peroxin interactions using a non-transcription-based bacterial two-hybrid assay. Mol Cell Proteomics 2002, 1:243-252. https://dx.doi.org/10.1074/mcp.m100025-mcp200

40. Li F, Xu D, Wang Y, Zhou Z, Liu J, Hu S, Gong Y, Yuan J, Pan L. Structural insights into the ubiquitin recognition by OPTN (optineurin) and its regulation by TBK1-mediated phosphorylation. Autophagy 2018, 14:66-79. https://dx.doi.org/10.1080/15548627.2017.1391970

41. Turturro S, Shen X, Shyam R, Yue BY, Ying H. Effects of mutations and deletions in the human optineurin gene. Springerplus 2014, 3:99. https://dx.doi.org/10.1186/2193-1801-3-99.

42. Itoh R, Fujiki Y. Functional domains and dynamic assembly of the peroxin Pex14p, the entry site of matrix proteins. J Biol Chem 2006, 281: 10196-10205. https://dx.doi.org/10.1074/jbc.M600158200

43. McEwan DG, Dikic I. The three musketeers of autophagy: phosphorylation, ubiquitylation and acetylation. Trends Cell Biol 2011, 21:195-201. https://dx.doi.org/10.1016/j.tcb.2010.12.006

44. Richter B, Sliter DA, Herhaus L, Stolz A, Wang C, Beli P, Zaffagnini G, Wild P, Martens S, Wagner SA, Youle RJ, Dikic I. Phosphorylation of OPTN by TBK1 enhances its binding to Ub chains and promotes selective autophagy of damaged mitochondria. Proc Natl Acad Sci USA 2016, 113:4039-4044. https://dx.doi.org/10.1073/pnas.1523926113

45. Waterham HR, Koster J, Ebberink MS, Ješina P, Zeman J, Nosková L, Kmoch S, Devic P, Cheillan D, Wanders RJA, Ferdinandusse S. Autosomal dominant Zellweger spectrum disorder caused by de novo variants in PEX14 gene. Genet Med 2023, 25:100944. https://dx.doi.org/10.1016/j.gim.2023.100944

46. Vittitow J, Borrás T. Expression of optineurin, a glaucoma-linked gene, is influenced by elevated intraocular pressure. Biochem Biophys Res Commun 2002, 298:67-74. https://dx.doi.org/10.1016/s0006-291x(02)02395-1

47. Sudhakar C, Vaibhava V, Swarup G. IRF-1-binding site in the first intron mediates interferon-γ-induced optineurin promoter activation. Biochem Biophys Res Commun 2013, 437:179-184. https://dx.doi.org/10.1016/j.bbrc.2013.06.065

48. Dutta RK, Maharjan Y, Lee JN, Park C, Ho YS, Park R. Catalase deficiency induces reactive oxygen species mediated pexophagy and cell death in the liver during prolonged fasting. Biofactors 2021, 47:112-125. https://dx.doi.org/10.1002/biof.1708

## Methods-only references

49. Nordgren M, Wang B, Apanasets O, Brees C, Veldhoven PP, Fransen M. Potential limitations in the use of KillerRed for fluorescence microscopy. J Microsc 2012, 245:229-235. https://dx.doi.org/10.1111/j.1365-2818.2011.03564.x

50. Will GK, Soukupova M, Hong X, Erdmann KS, Kiel JA, Dodt G, Kunau WH, Erdmann R. Identification and characterization of the human orthologue of yeast Pex14p. Mol Cell Biol 1999, 19:2265-2277. https://dx.doi.org/10.1128/MCB.19.3.2265

51. Fransen M, Vastiau I, Brees C, Brys V, Mannaerts GP, Van Veldhoven PP. Potential role for Pex19p in assembly of PTS-receptor docking complexes. J Biol Chem 2004, 279:12615-12624. https://dx.doi.org/10.1074/jbc.M304941200

52. Walton PA, Brees C, Lismont C, Apanasets O, Fransen M. The peroxisomal import receptor PEX5 functions as a stress sensor, retaining catalase in the cytosol in times of

oxidative stress. Biochim Biophys Acta Mol Cell Res 2017, 1864:1833-1843. https://dx.doi.org/10.1016/j.bbamcr.2017.07.013

53. Kubala MH, Kovtun O, Alexandrov K, Collins BM. Structural and thermodynamic analysis of the GFP:GFP-nanobody complex. Protein Sci 2010, 19:2389-2401. https://dx.doi.org/10.1002/pro.519

54. Park BC, Shen X, Samaraweera M, Yue BY. Studies of optineurin, a glaucoma gene: Golgi fragmentation and cell death from overexpression of wild-type and mutant optineurin in two ocular cell types. Am J Pathol 2006, 169:1976-1989. https://dx.doi.org/10.2353/ajpath.2006.060400

55. Lismont C, Nordgren M, Brees C, Knoops B, Van Veldhoven PP, Fransen M. Peroxisomes as modulators of cellular protein thiol oxidation: a new model system. Antioxid Redox Signal 2019, 30:22-39. https://dx.doi.org/10.1089/ars.2017.6997

56. Campeau E, Ruhl VE, Rodier F, Smith CL, Rahmberg BL, Fuss JO, Campisi J, Yaswen P, Cooper PK, Kaufman PD. A versatile viral system for expression and depletion of proteins in mammalian cells. PLoS One 2009, 4:e6529. https://dx.doi.org/10.1371/journal.pone.0006529

57. Bhalla K, Rosier K, Monnens Y, Meulemans S, Vervoort E, Thorrez L, Agostinis P, Meier DT, Rochtus A, Resnick JL, Creemers JWM. Similar metabolic pathways are affected in both Congenital Myasthenic Syndrome-22 and Prader-Willi Syndrome. Biochim Biophys Acta Mol Basis Dis 2024, 1870:167175. https://dx.doi.org/10.1016/j.bbadis.2024.167175

58. Boussif O, Lezoualc'h F, Zanta MA, Mergny MD, Scherman D, Demeneix B, Behr JP. A versatile vector for gene and oligonucleotide transfer into cells in culture and in vivo: polyethylenimine. Proc Natl Acad Sci USA 1995, 92:7297-7301. https://dx.doi.org/10.1073/pnas.92.16.7297

59. Fransen M, Wylin T, Brees C, Mannaerts GP, Van Veldhoven PP. Human pex19p binds peroxisomal integral membrane proteins at regions distinct from their sorting sequences. Mol Cell Biol 2001, 21:4413-4424. https://dx.doi.org/10.1128/MCB.21.13.4413-4424.2001

60. Amery L, Fransen M, De Nys K, Mannaerts GP, Van Veldhoven PP. Mitochondrial and peroxisomal targeting of 2-methylacyl-CoA racemase in humans. J Lipid Res 2000, 41:1752-1759. https://dx.doi.org/10.1016/S0022-2275(20)31968-4

61. Van Veldhoven PP, de Schryver E, Young SG, Zwijsen A, Fransen M, Espeel M, Baes M, Van Ael E. Slc25a17 gene trapped mice: PMP34 plays a role in the peroxisomal degradation of phytanic and pristanic acid. Front Cell Dev Biol 2020, 8:144. https://dx.doi.org/10.3389/fcell.2020.00144

62. Schneider CA, Rasband WS, Eliceiri KW. NIH Image to ImageJ: 25 years of image analysis. Nat Methods 2012, 9:671-675. https://dx.doi.org/10.1038/nmeth.2089

63. Ramazani Y, Knops N, Berlingerio SP, Adebayo OC, Lismont C, Kuypers DJ, Levtchenko E, van den Heuvel LP, Fransen M. Therapeutic concentrations of calcineurin inhibitors do not deregulate glutathione redox balance in human renal proximal tubule cells. PLoS One 2021, 16:e0250996. https://dx.doi.org/10.1371/journal.pone.0250996

64. Huybrechts SJ, Van Veldhoven PP, Brees C, Mannaerts GP, Los GV, Fransen M. Peroxisome dynamics in cultured mammalian cells. Traffic 2009, 10:1722-1733. https://dx.doi.org/10.1111/j.1600-0854.2009.00970.x

65. Käll L, Canterbury JD, Weston J, Noble WS, MacCoss MJ. Semi-supervised learning for peptide identification from shotgun proteomics datasets. Nat Methods 2007, 4:923-925. https://dx.doi.org/10.1038/nmeth1113

66. Claes Z, Bollen M. A split-luciferase lysate-based approach to identify small-molecule modulators of phosphatase subunit interactions. Cell Chem Biol 2023, 30:1666-1679. https://dx.doi.org/10.1016/j.chembiol.2023.07.018

67. Rothbauer U, Zolghadr K, Muyldermans S, Schepers A, Cardoso MC, Leonhardt H. A versatile nanotrap for biochemical and functional studies with fluorescent fusion proteins. Mol Cell Proteomics 2008, 7:282-289. https://dx.doi.org/10.1074/mcp.M700342-MCP200

68. Mirdita M, Schütze K, Moriwaki Y, Heo L, Ovchinnikov S, Steinegger M. ColabFold: making protein folding accessible to all. Nat Methods 2022, 19:679-682. https://dx.doi.org/10.1038/s41592-022-01488-1

69. Kachaner D, Génin P, Laplantine E, Weil R. Toward an integrative view of optineurin functions. Cell Cycle 2012, 11:2808-2818. https://dx.doi.org/10.4161/cc.20946

70. Swarup G, Sayyad Z. Altered functions and interactions of glaucoma-associated mutants of optineurin. Front Immunol 2018,9:1287. https://dx.doi.org/10.3389/fimmu.2018.01287

71. Weil R, Laplantine E, Curic S, Génin P. Role of optineurin in the mitochondrial dysfunction: potential implications in neurodegenerative diseases and cancer. Front Immunol 2018, 9:1243. https://dx.doi.org/10.3389/fimmu.2018.01243

72. Zhao S, Chen R, Gao Y, Lu Y, Bai X, Zhang J. Fundamental roles of the optineurin gene in the molecular pathology of amyotrophic lateral sclerosis. Front Neurosci 2023, 17:1319706. https://dx.doi.org/10.3389/fnins.2023.1319706

## Figure legends

**Fig. 1: Cell type-specific recruitment of optineurin to peroxisomes. a**, Distribution patterns of OPTN-GFP and mCherry-PTS1 in four distinct cell lines, either co-expressing (right panels) or not (left panels) a high-affinity plasma membrane-targeted anti-GFP nanobody ($GFP_{Nb}$-PM). Before analysis, the cells were incubated for 2 h with 200 nM BafA1. Representative images are shown. The white arrowheads indicate colocalization of OPTN-GFP and mCherry-PTS1. The yellow arrowheads indicate positions where peroxisomes are associated with the plasma membrane. **b**, Enlargements of the boxed areas in panel a. **c**, Distribution patterns of endogenous PEX14 and OPTN in HEK-293 and HCT116 cells. **d**, High-resolution imaging and volume rendering of two mCherry-PTS1/OPTN-GFP aggregates in HEK-293 cells. Scale bars: **a-c**, 10 µm; **d**, 500 nm.

**Fig. 2: PEX14 is a proximity partner of OPTN. a**, Schematic representation of the distinct domains and major interactions of the miniTurbo-OPTN-GFP fusion protein. ATG9A, autophagy-related protein 9A; CC, coiled-coil; CYLD, cylindromatosis; HLH, helix-loop-helix; HTT, huntingtin; LZ, leucine zipper domain; LC3/GABARAP, microtubule-associated protein 1A/1B-light chain 3/γ-aminobutyric acid receptor-associated protein; LIR, LC3-interacting region; Rab, Ras-related protein; TBC1D17, TBC1 domain family member 17; TBK1, TANK (TRAF-associated NF-kB activator) binding kinase 1; UBD, ubiquitin-binding domain; ZF, zinc finger. **b**, Volcano plot displaying the $Log_2$-fold changes (FC) in protein abundance alongside the corresponding $Log_{10}$-fold adjusted p-values (pAdj) for 2856 proteins obtained through streptavidin-affinity purification and identification/quantification by LC–MS/MS. The analysis was performed on miniTurbo-OPTN-GFP-expressing HEK-293 cells (n = 4 biological replicates), assayed under conditions with or without 50 µM biotin. Green, blue, and red dots represent miniTurbo-OPTN-GFP, known OPTN interaction partners, and bona fide peroxisomal proteins that could be identified in the affinity-purified fractions. Vertical and horizontal dotted lines denote the FC (2x) and pAdj (0.05) cut-offs, respectively.

**Fig. 3: Mapping of PEX14-interacting and pexophagy-inducing regions of OPTN.** Flp-In T-REx 293 cells stably expressing po-mKeima were transfected with a plasmid encoding the indicated GFP-fusion protein and cultured in regular DMEM medium. After two days, the cells were harvested and processed for GFP-Trap and FACS analyses. To measure the percentage of cells undergoing pexophagy, single-cell GFP-positive populations were gated

for a decrease in fluorescence intensity in the neutral channel. **a**, Samples of protein extracts (input) and the GFP Trap were processed for SDS-PAGE followed by immunoblotting using antibodies to GFP, PEX14, and GAPDH. Representative blots are shown. Specific protein bands are marked by arrows. Molecular mass markers (in kDa) are indicated on the left. **b**, Densitometry quantifications of the relative ratios (RR) of PEX14/GFP and PEX14/OPTN-GFP fusion proteins retained on the GFP-Trap affinity matrix. The total signal intensities of the GFP proteins and PEX14 were both standardized to 100%. The bars represent the mean of 3 biological replicates. The densitometry quantifications of the relative normalized amounts (R-NA) of the proteins under study in the soluble extract input fractions are shown in the Extended Data Fig. 8. **c**, Examples of po-mKeima-expressing cells displaying no, weak, moderate, or excessively high levels of pexophagy. The visuals depict overlay images of po-mKeima excited at 440 nm (false color: green) or 586 nm (false color: red). Yellowish (=low 586/440 excitation peak ratio) and reddish (=high 586/440 excitation peak ratio) dots represent peroxisomes and autolysosomes, respectively [25]. Scale bar, 10 µm. **d**, Representative flow cytometry plots of each group (n = 3). The different colors represent the cell density at a given position. **e**, Quantification of the percentage of cells in the gated area. The data are shown as the mean ± SD and represent the values of 3 independent biological replicates. All conditions were statistically compared to the $OPTN_{1-577}$-GFP condition (ns, non-significant; *, $p < 0.05$; **, $p < 0.01$; ****, $p < 0.0001$).

**Fig. 4: OPTN-GFP interacts with PEX14 and triggers pexophagy in a UBD-dependent but ubiquitin-independent manner.** Flp-In T-REx 293 cells stably expressing po-mKeima were transfected with a plasmid encoding the indicated GFP-fusion protein and cultured in regular DMEM medium. After two days, the cells were harvested and processed for GFP-Trap and FACS analyses. To measure the percentage of cells undergoing pexophagy, single-cell GFP-positive populations were gated for a decrease in fluorescence intensity in the neutral channel. **a**,**c** Samples of protein extracts (input) and the GFP-Trap were processed for SDS-PAGE followed by immunoblotting using antibodies to GFP, PEX14, and GAPDH. Representative blots are shown. Specific protein bands are marked by arrows. Molecular mass markers (in kDa) are indicated on the left. **b**,**d** Densitometry quantifications of the relative ratios (RR) of PEX14/GFP and PEX14/OPTN-GFP fusion proteins retained on the GFP-Trap affinity matrix. The total signal intensities of the GFP proteins and PEX14 were both

standardized to 100%. The bars represent the mean of 3 biological replicates. The densitometry quantifications of the relative normalized amounts (R-NA) of the proteins under study in the soluble extract input fractions are shown in the Extended Data Fig. 8. **e**, Representative flow cytometry plots of each group (n = 3). The different colors represent the cell density at a given position. **f**, Quantification of the percentage of cells in the gated area. The data are shown as the mean ± SD and represent the values of 3 independent biological replicates. All conditions were statistically compared to the $OPTN_{1-577}$-GFP condition (ns, non-significant; *, $p < 0.05$; **, $p < 0.01$; ****, $p < 0.0001$).

**Fig. 5: $OPTN_{217-577}$-GFP-induced pexophagy in HEK-293 cells relies on endogenous OPTN.** Flp-In T-REx 293 cells, stably expressing po-mKeima, were transfected with either a control (CT) or OPTN siRNA and seeded in 6-well plates. On day 2, the cells were transfected with either a GFP- or $OPTN_{217-577}$-GFP-encoding plasmid. On day 3, the cells were transfected again with either siRNA CT or siRNA OPTN. On day 4, the cells were harvested and processed for FACS analysis. To measure the percentage of cells undergoing pexophagy, single-cell GFP-positive populations were gated for a decrease in fluorescence intensity in the neutral channel. **a**, Representative flow cytometry plots of each group (n = 3). The different colors represent the cell density at a given position. **b**, Quantification of the percentage of cells in the gated area. The data are shown as the mean ± SD and represent the values of 3 independent biological replicates. The impact of OPTN downregulation and $OPTN_{217-577}$-GFP overexpression were statistically compared (ns, non-significant; *, $p < 0.05$; **, $p < 0.01$;****, $p < 0.0001$).

**Fig. 6: Mapping of the OPTN-interacting region of PEX14 and assessment of its expression levels on OPTN-mediated pexophagy.** Flp-In T-REx 293 cells stably expressing po-mKeima were (co-)transfected with (a) plasmid(s) encoding the indicated protein(s) and cultured in regular DMEM medium. After two days, the cells were harvested and processed for GFP-Trap and FACS analysis. To measure the percentage of cells undergoing pexophagy, single-cell GFP-positive populations were gated for a decrease in fluorescence intensity in the neutral channel. **a**, Samples of protein extracts (input) and the GFP-Trap were processed for SDS-PAGE followed by immunoblotting using antibodies to GFP, OPTN, and GAPDH. Representative blots are shown. Specific protein bands are marked by arrows. Molecular mass markers (in kDa) are indicated on the left. **b**, Densitometry quantifications of the

relative ratios (RR) of OPTN/GFP and OPTN/PEX14-GFP fusion proteins retained on the GFP-Trap affinity matrix. The total signal intensities of the GFP proteins and PEX14 were both standardized to 100%. The bars represent the mean of 3 biological replicates. The densitometry quantifications of the relative normalized amounts (R-NA) of the proteins under study in the soluble extract input fractions are shown in the Extended Data Fig. 8. **c**,**e**, Representative flow cytometry plots of each group (n = 2-3). The different colors represent the cell density at a given position. **d**,**f**, Quantification of the percentage of cells in the gated area. The data are shown as the mean ± SD and represent the values of 2-3 independent biological replicates. Relevant conditions were statistically compared (ns, non-significant; ***, $p < 0.001$).

## Extended Data Figure legends

**Extended Data Fig. 1: Expression of OPTN-GFP triggers pexophagy in HCT116 but not in HeLa cells.** HCT116 and HeLa cells stably expressing po-mKeima were transfected with a plasmid encoding GFP or OPTN-GFP and cultured as described in the Materials and Methods section. After two days, the cells were harvested and processed for FACS analysis. To measure the percentage of cells undergoing pexophagy, single-cell GFP-positive populations were gated for a decrease in fluorescence intensity in the neutral channel. **a**, Representative flow cytometry plots of each group (n = 3). The different colors represent the cell density at a given position. **b**, Quantification of the percentage of cells in the gated area. The data are shown as the mean ± SD and represent the values of 3 independent biological replicates. All conditions were statistically compared to the GFP condition (ns, non-significant; **, $p < 0.01$).

**Extended Data Fig. 2: Effect of OPTN-GFP on organelle morphology in HEK-293 cells. a**, MitoTracker™ Red CM-H2Xros (MT) and ER-Tracker™ Blue-White DPX (ER) staining. **b**, LysoTracker™ Red DND-99 (LY) staining. Before live cell imaging, cells were incubated for 2 h with 200 nM BafA1. Representative images are shown. The lower panels depict enlargements of the boxed areas in the upper panels. Scale bars, 10 µm.

**Extended Data Fig. 3: Analysis of the OPTN-PEX14 interaction using GFP-trapping. a**, Immunoblot analysis of input and GFP-Trap pull-down fractions from Flp-In T-REx 293 cells expressing the specified proteins. Representative images are shown. Specific protein bands and their degradation products are marked by arrows and arrowheads, respectively. Molecular mass markers (in kDa) are indicated on the left. **b**, Densitometry quantifications of the relative ratios (RR) of PEX14/GFP and PEX14/OPTN-GFP retained on the GFP-Trap affinity matrix. The total signal intensities of the GFP proteins and PEX14 were both standardized to 100%. The bars represent the mean of 2 biological replicates. The densitometry quantifications of the relative normalized amounts (R-NA) of the proteins under study in the soluble extract input fractions are shown in the Extended Data Fig. 8. T, transient transfection; F, Flp-In integration; L, lentiviral transduction.

**Extended Data Fig. 4: Relative expression of GFP-tagged OPTN compared to endogenous OPTN in lentiviral-transduced Flp-In T-REx 293 cells.** Total cell lysates from lentiviral (L-)

transduced Flp-In T-REx 293 cells, which constitutively express either GFP or OPTN-GFP, were subjected to SDS-PAGE followed by immunoblotting using antibodies targeting OPTN and GAPDH. **a**, A representative image is shown, with specific protein bands indicated by arrows. Note that the 66 kDa band in the OPTN-GFP lane may represent either a degradation product of OPTN-GFP or endogenous OPTN stabilized by overexpression of OPTN-GFP. Molecular mass markers (in kDa) are indicated on the left. **b**, Densitometry quantifications of the relative normalized amounts (R-NA) of OPTN. The expression levels were normalized to GAPDH, with the amount of OPTN detected in the GFP cells serving as the reference. The amount in the L-OPTN-GFP cells represents the sum of the 66 and 95 kDa bands. The bars represent the mean of 4 biological replicates.

**Extended Data Fig. 5: Validation of the effectiveness of the OPTN DsiRNA.** Flp-In T-REx 293 cells stably expressing po-mKeima were transfected with either a control (CT) or OPTN DsiRNA and seeded in 6-well plates. On day 2, the cells were transfected or not with a plasmid encoding $OPTN_{217-577}$-GFP. On day 3, the cells were transfected again with either siRNA CT or siRNA OPTN. On day 4, the cells were harvested and processed for immunoblotting with antisera raised against the indicated proteins. **a**, Representative blots showing the effectiveness of the OPTN DsiRNA. Specific protein bands are marked by arrows. **b**, Densitometry quantifications of the relative normalized amounts (R-NA) of the OPTN levels shown in panel a (n = 3). **c**, Comparison of the migration behavior of endogenous OPTN (CT DsiRNA condition) and $OPTN_{217-577}$-GFP (OPTN DsiRNA / $OPTN_{217-577}$-GFP condition). Molecular mass markers (in kDa) are indicated on the left.

**Extended Data Fig. 6: Structural modeling of the OPTN-OPTN-PEX14 complex. a**, Structural model of the OPTN-OPTN-PEX14 complex before (left) and after (right) a 50 ns molecular dynamics (MD) simulation, depicted in either cartoon or surface representation. Residues were colored as follows: OPTN $_{420-510}$ in green (2x), and PEX14 in red (residues 1-137) and blue (residues 138-200). **b**, RMSD plot during MD simulations for the protein-protein complex.

**Extended Data Fig. 7: Structural dynamics and modeling parameters of the OPTN-OPTN-PEX14 complex. a**, Illustration of the multiple-sequence alignment coverage of the OPTN-OPTN-PEX14 sequence used as input for predicting the complex structure. The black line represents the total coverage for each residue. Residues corresponding to $OPTN_{420–510}$

(proteins A and B) and $PEX14_{1-200}$ (protein C) are indicated. **b**, Plot of the pLDDT scores for the top-ranked 5 structural models. Each model is depicted in a different color. **c**, Free energy landscape, **d**, RMSF, **e**, hydrogen bond, **f**, gyrate, and **g**, SASA changes during molecular dynamics simulations.

**Extended Data Fig. 8: Densitometry quantification of proteins in soluble extract input fractions used for the GFP-Trap analyses in this study.** A portion of the soluble extracts from Flp-In T-REx 293 cells (co-)transfected with (a) plasmid(s) encoding the proteins of interest, and used for GFP-Trap assays, were processed for immunoblotting with antibodies specific for the indicated proteins. The expression levels were normalized to GAPDH, with the amount of protein found in cells transiently transfected with a plasmid encoding GFP serving as the reference. (**a**, **b**, **c**, **d**) Representative examples of soluble extract input fractions used to conduct the experiments shown in Figs. 3, 4, 6, and Extended Fig. 3, respectively.

**Extended Data Table 1: Binding affinities of protein-protein interactions by MMPBSA (kcal/mol).** $\Delta E_{vdw}$: van der Waals energy; $\Delta E_{ele}$: electrostatic energy; $\Delta G_{GB}$: polar contribution to solvation; $\Delta G_{SA}$: no-polar contribution to solvation; $\Delta G_{binding}$: binding free energy. A, $OPTN_{420–510}$; B, $OPTN_{420–510}$; C, $PEX14_{1-200}$.

**Extended Data Movie 1: Trajectory tracking of molecular dynamics simulations for the OPTN-OPTN-PEX14 complex.**

## Supplementary Figure legends

**Supplementary Fig. 1: Schematic overview of the nanobody-driven plasma membrane translocation assay for visualizing protein-protein interactions in living cells.** Co-transfection of cells with three plasmids encoding a GFP-tagged protein (bait), an mCherry-tagged protein (prey), and a high-affinity anti-GFP nanobody with a plasma membrane-targeting motif ($GFP_{Nb}$-PM) enables interaction visualization through co-imaging of their subcellular localization. Upon interaction, both the bait and prey proteins are recruited to the plasma membrane, while in the absence of interaction, only the bait protein localizes to the plasma membrane.

**Supplementary Fig. 2: Schematic overview of the proximity-dependent biotin labeling procedure.**

Fig. 1

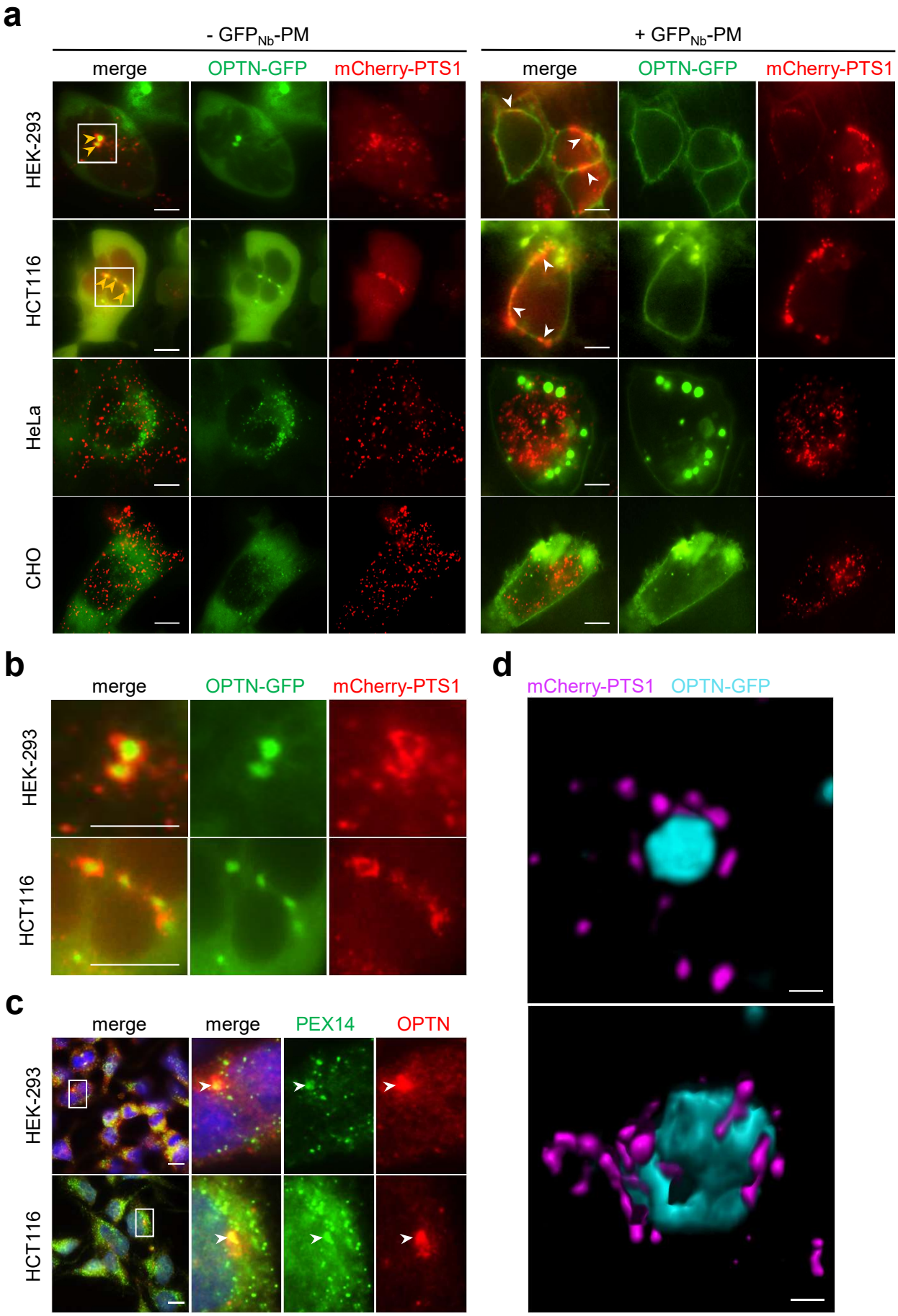
a
- GFP$_{Nb}$-PM
+ GFP$_{Nb}$-PM
merge
OPTN-GFP
mCherry-PTS1
HEK-293
HCT116
HeLa
CHO
b
c
merge
PEX14
OPTN
d
mCherry-PTS1
OPTN-GFP

**Fig. 2**

**a**

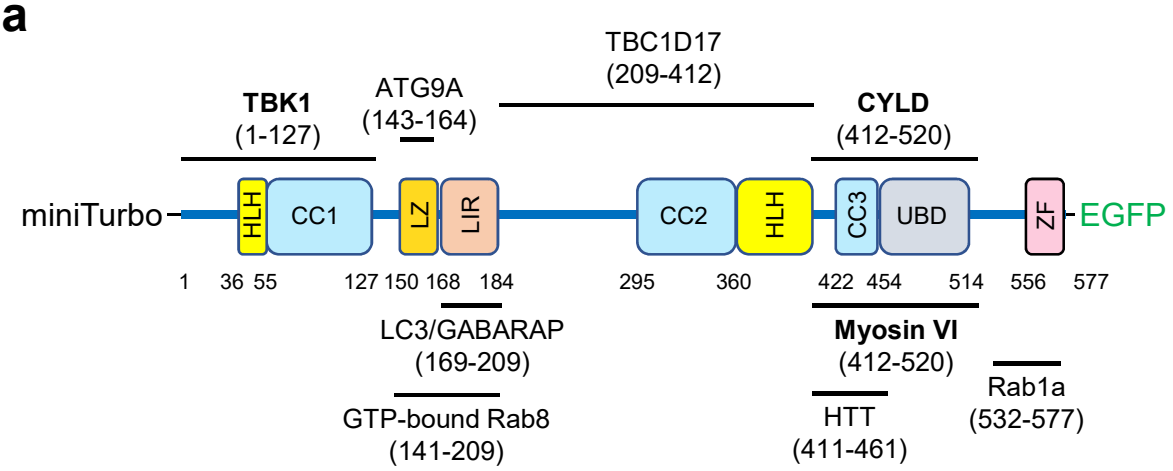
TBC1D17
(209-412)
TBK1
(1-127)
ATG9A
(143-164)
CYLD
(412-520)
miniTurbo
HLH
CC1
LZ
LIR
CC2
HLH
CC3
UBD
ZF
EGFP
1 36 55 127 150 168 184 295 360 422 454 514 556 577
LC3/GABARAP
(169-209)
GTP-bound Rab8
(141-209)
Myosin VI
(412-520)
HTT
(411-461)
Rab1a
(532-577)

**b**

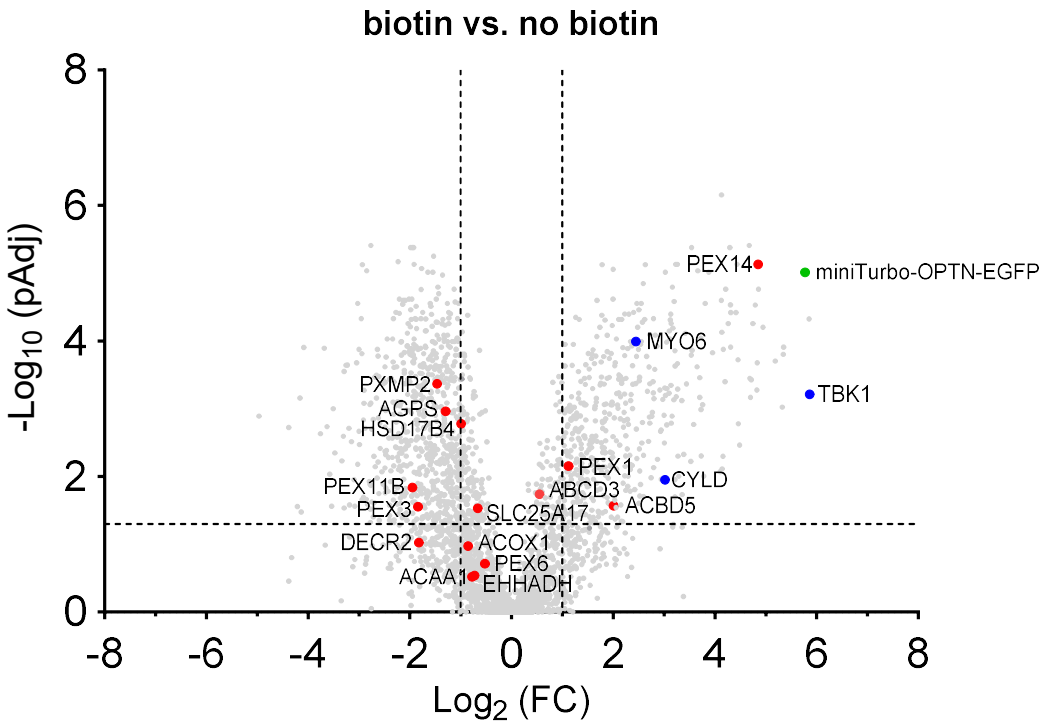
biotin vs. no biotin
-Log10 (pAdj)
Log2 (FC)
8
6
4
2
0
-8
-6
-4
-2
0
2
4
6
8
PEX14
miniTurbo-OPTN-EGFP
MYO6
TBK1
PXMP2
AGPS
HSD17B4
PEX1
CYLD
PEX11B
ABCD3
ACBD5
PEX3
SLC25A17
DECR2
ACOX1
PEX6
ACAA1
EHHADH

# Fig. 3

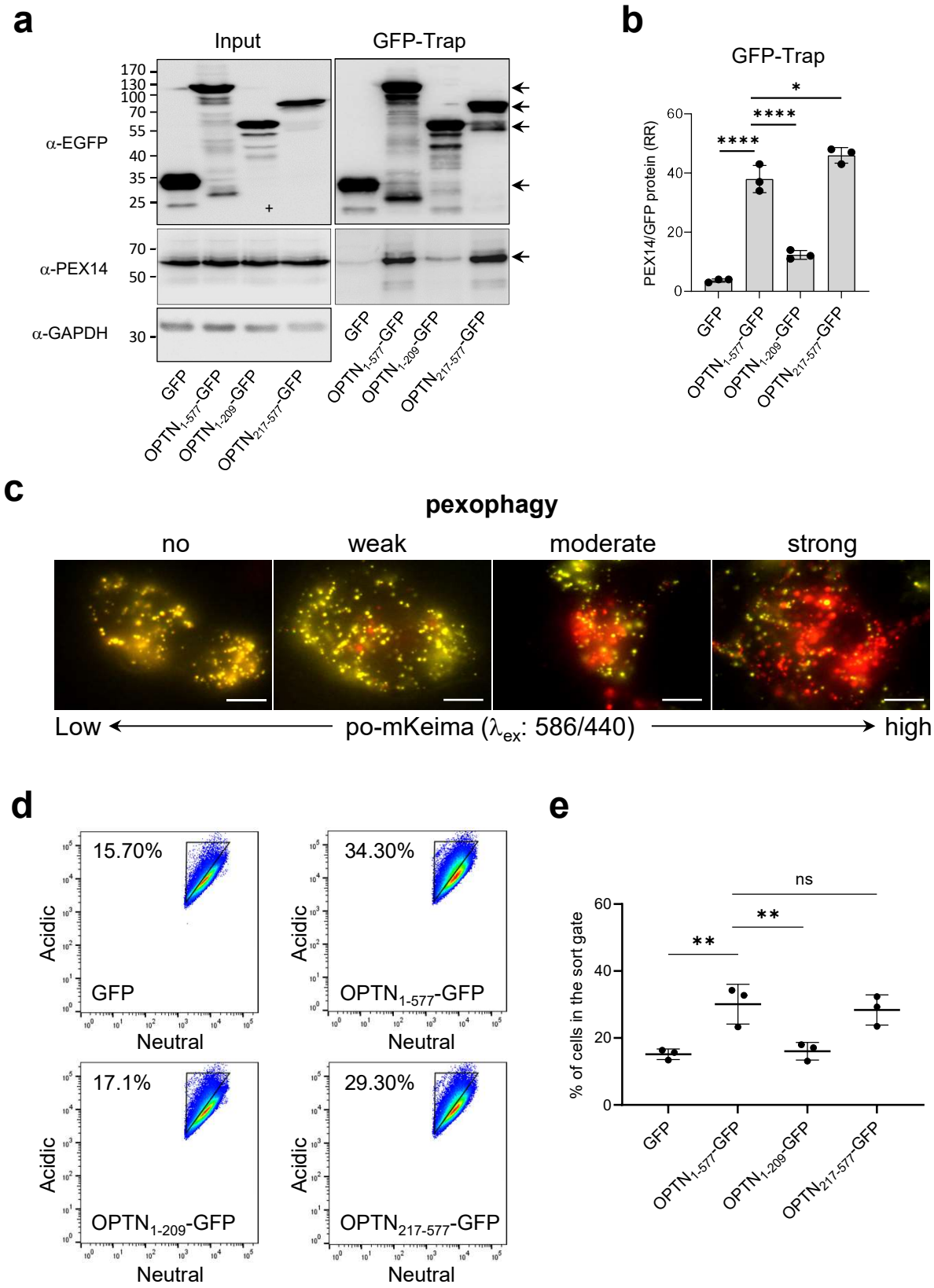
a
Input
GFP-Trap
170
130
100
70
55
40
35
25
α-EGFP
70
50
α-PEX14
30
α-GAPDH
GFP
OPTN1-577-GFP
OPTN1-209-GFP
OPTN217-577-GFP
b
GFP-Trap
PEX14/GFP protein (RR)
60
40
20
0
****
****
*
c
pexophagy
no
weak
moderate
strong
Low
po-mKeima (λex: 586/440)
high
d
15.70%
GFP
34.30%
OPTN1-577-GFP
17.1%
OPTN1-209-GFP
29.30%
OPTN217-577-GFP
Acidic
Neutral
e
% of cells in the sort gate
ns
**
**

Fig. 4

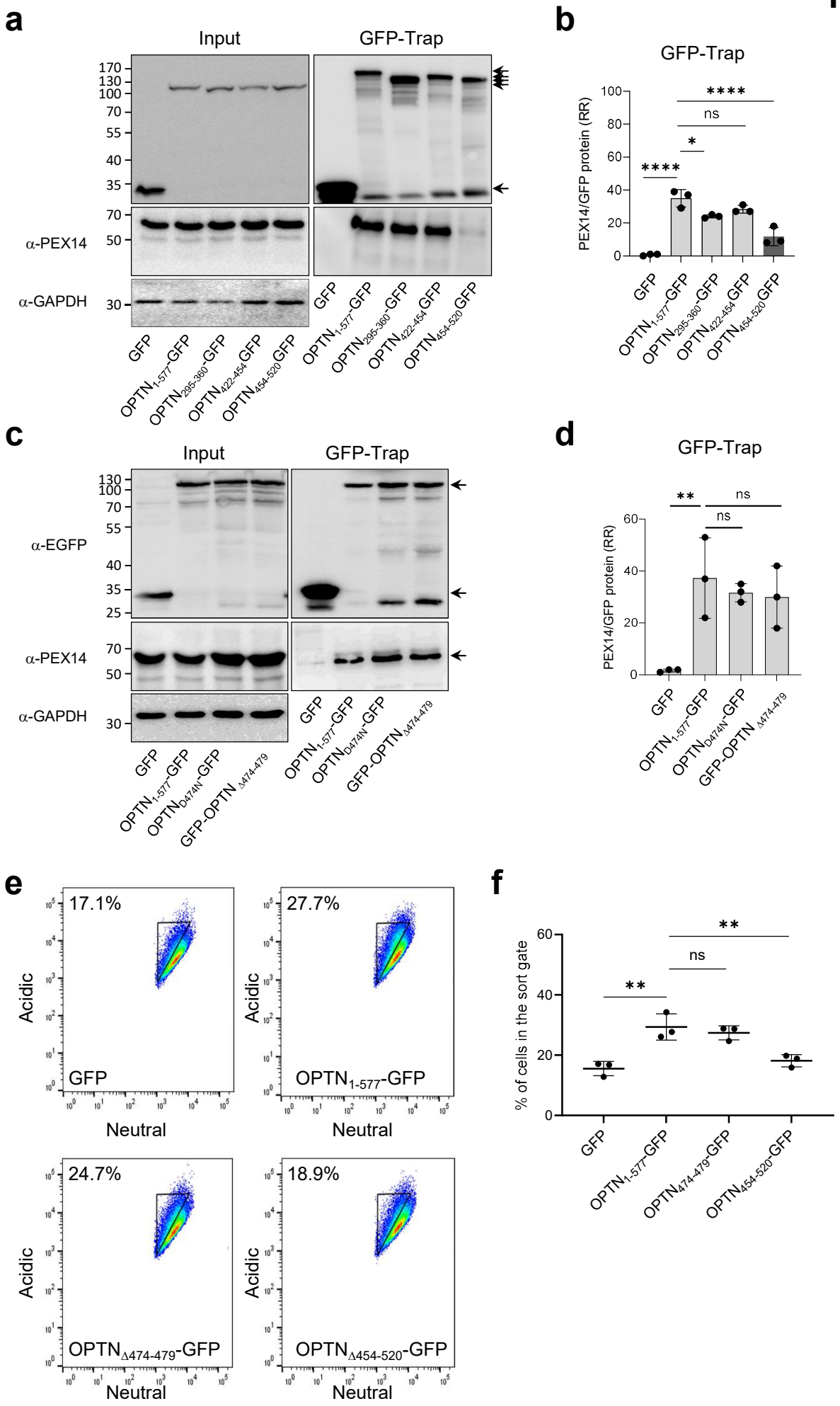
a
Input
GFP-Trap
170
130
100
70
55
40
35
70
50
30
α-PEX14
α-GAPDH
GFP
OPTN1-577-GFP
OPTN295-360-GFP
OPTN422-454-GFP
OPTN454-520-GFP
b
GFP-Trap
PEX14/GFP protein (RR)
100
80
60
40
20
0
****
ns
*
****
c
Input
GFP-Trap
130
100
70
55
40
35
25
70
50
30
α-EGFP
α-PEX14
α-GAPDH
GFP
OPTN1-577-GFP
OPTND474N-GFP
GFP-OPTN Δ474-479
d
GFP-Trap
PEX14/GFP protein (RR)
60
40
20
0
**
ns
ns
e
17.1%
GFP
27.7%
OPTN1-577-GFP
24.7%
OPTNΔ474-479-GFP
18.9%
OPTNΔ454-520-GFP
Acidic
Neutral
f
% of cells in the sort gate
60
40
20
0
**
ns
**
GFP
OPTN1-577-GFP
OPTN474-479-GFP
OPTN454-520-GFP

**Fig. 5**

**a**

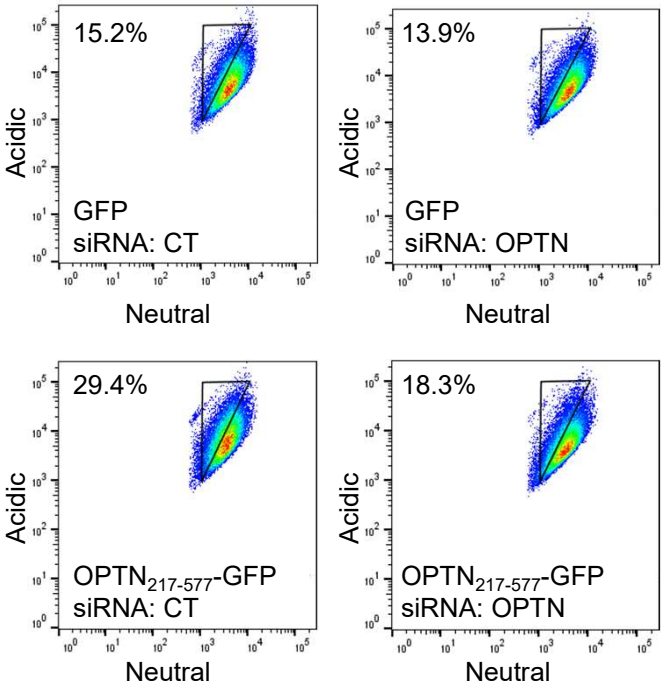
15.2%
GFP
siRNA: CT
13.9%
GFP
siRNA: OPTN
29.4%
OPTN217-577-GFP
siRNA: CT
18.3%
OPTN217-577-GFP
siRNA: OPTN
Acidic
Neutral

**b**

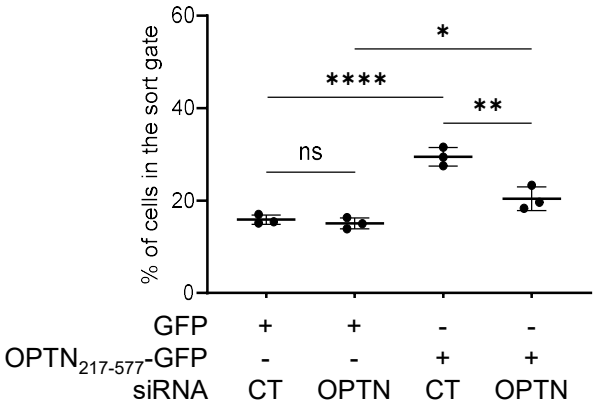
% of cells in the sort gate
60
40
20
0
*
****
**
ns
GFP + + - -
OPTN217-577-GFP - - + +
siRNA CT OPTN CT OPTN

# Fig. 6

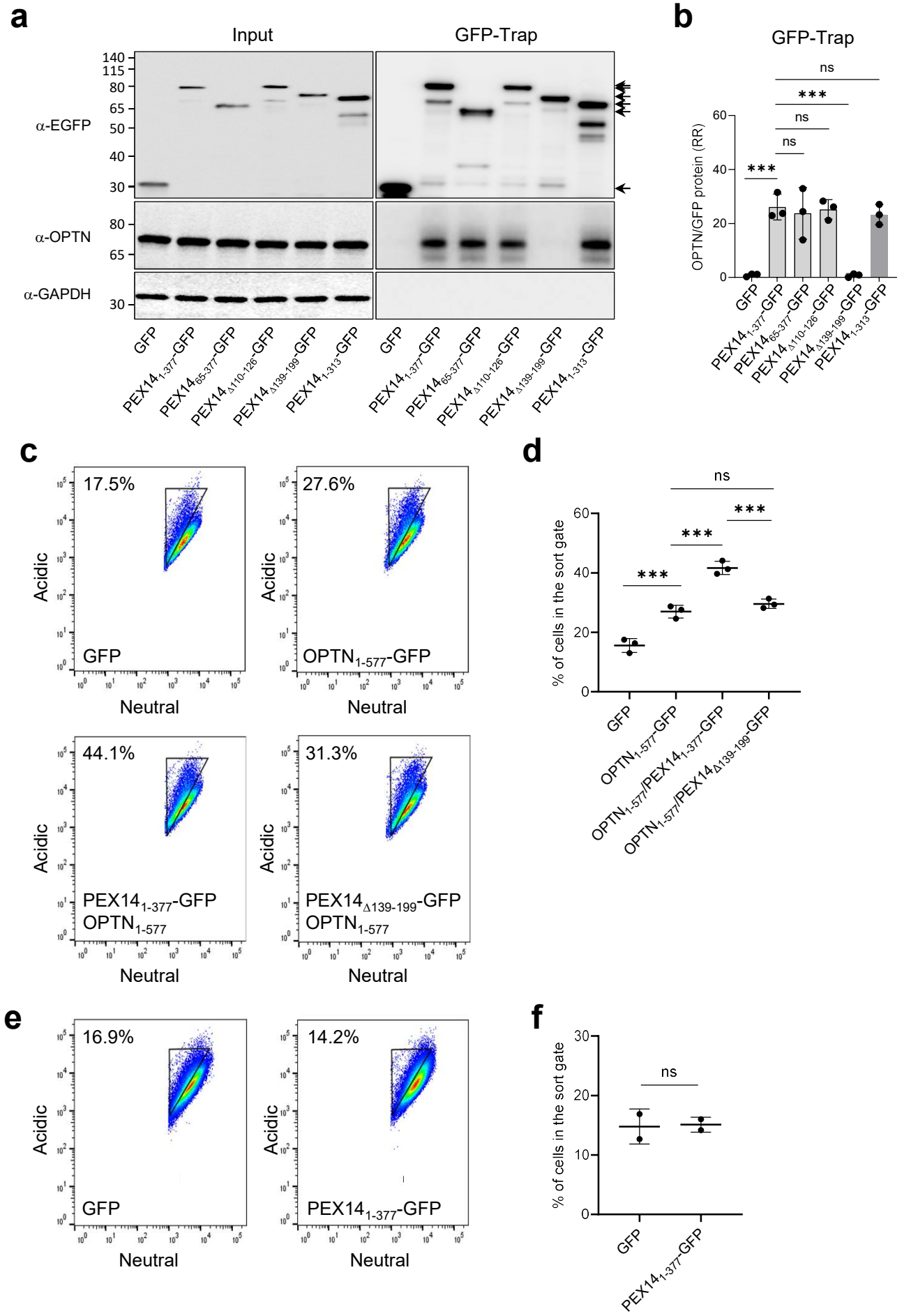
a
Input
GFP-Trap
α-EGFP
α-OPTN
α-GAPDH
140
115
80
65
50
40
30
GFP
PEX14$_{1-377}$-GFP
PEX14$_{65-377}$-GFP
PEX14$_{\Delta 110-126}$-GFP
PEX14$_{\Delta 139-199}$-GFP
PEX14$_{1-313}$-GFP
b
GFP-Trap
OPTN/GFP protein (RR)
ns
***
c
17.5%
GFP
27.6%
OPTN$_{1-577}$-GFP
44.1%
PEX14$_{1-377}$-GFP
OPTN$_{1-577}$
31.3%
PEX14$_{\Delta 139-199}$-GFP
OPTN$_{1-577}$
Acidic
Neutral
d
% of cells in the sort gate
OPTN$_{1-577}$-GFP
OPTN$_{1-577}$/PEX14$_{1-377}$-GFP
OPTN$_{1-577}$/PEX14$_{\Delta 139-199}$-GFP
e
16.9%
GFP
14.2%
PEX14$_{1-377}$-GFP
f

# Extended Data Fig. 1

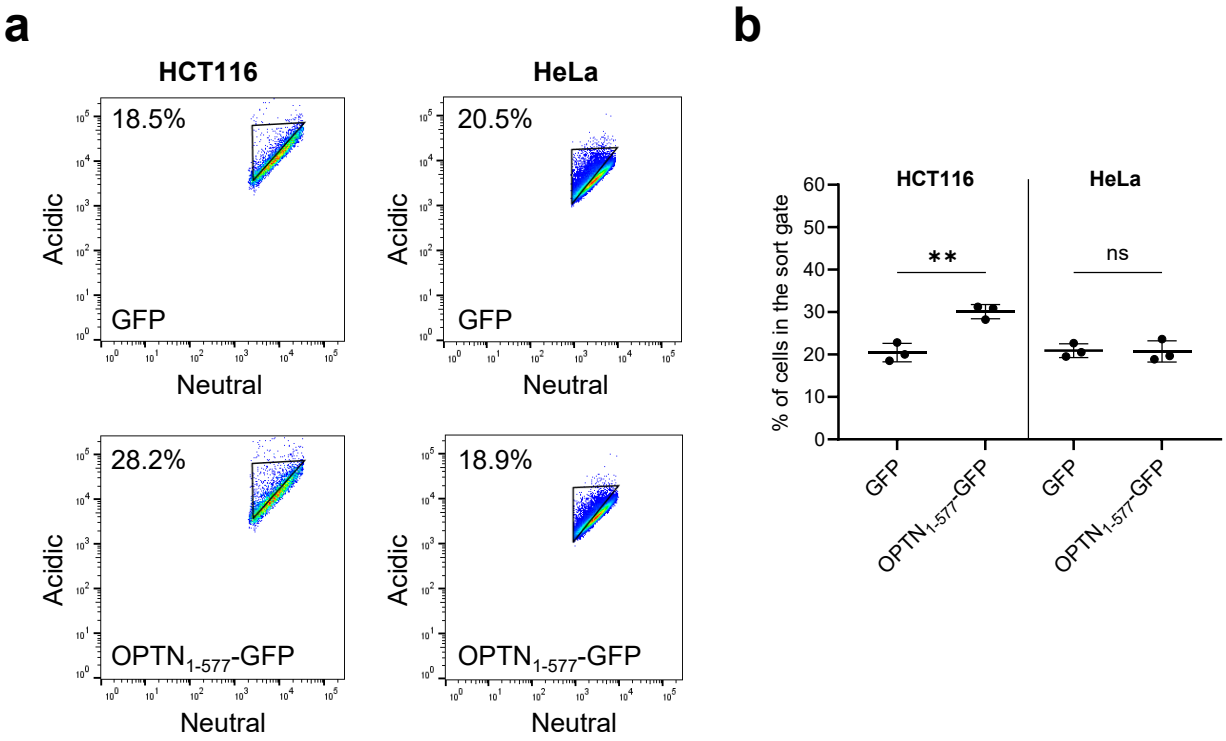

# Extended Data Fig. 2

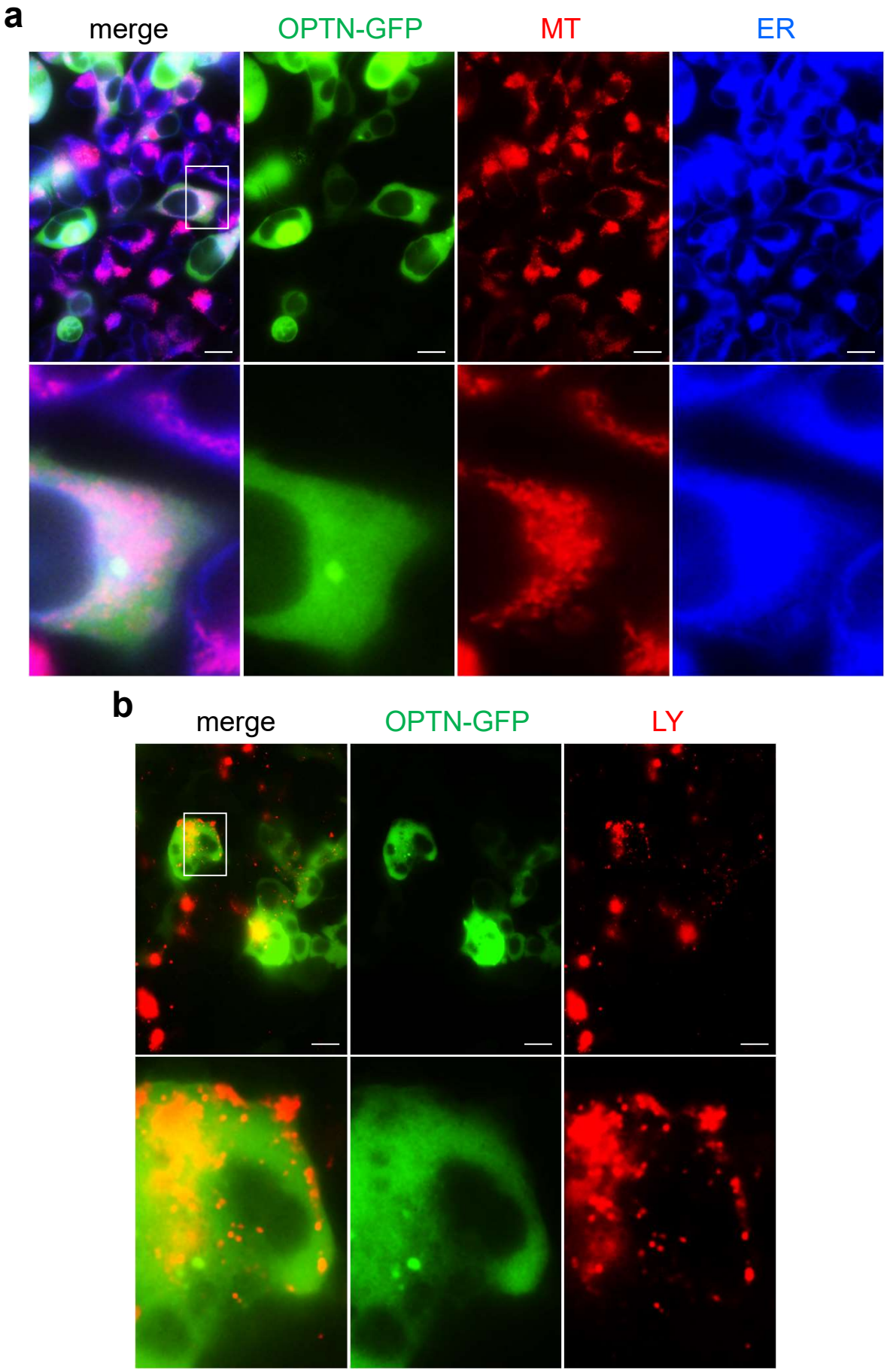

# Extended Data Fig. 3

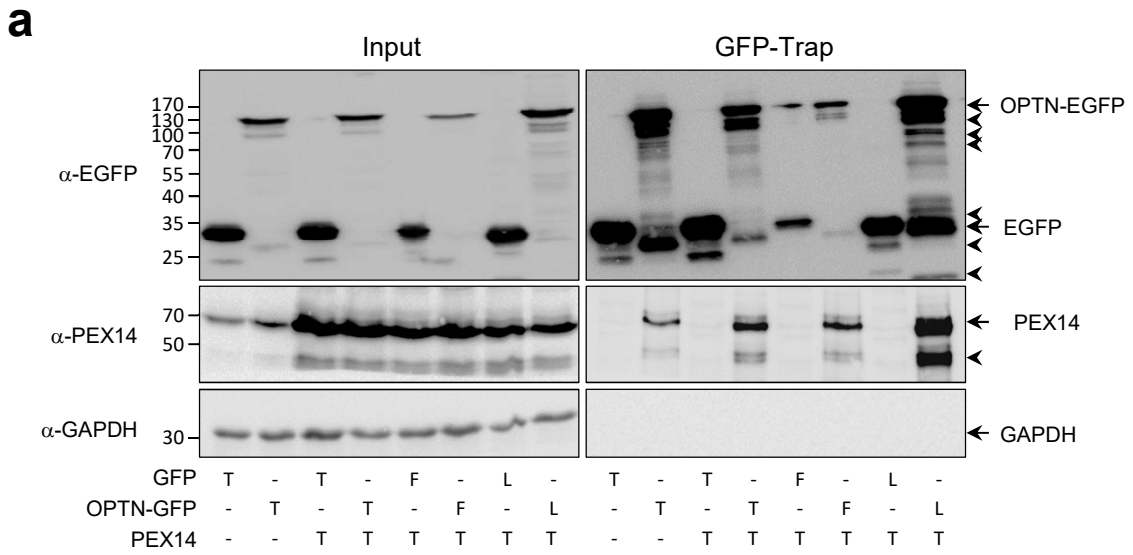


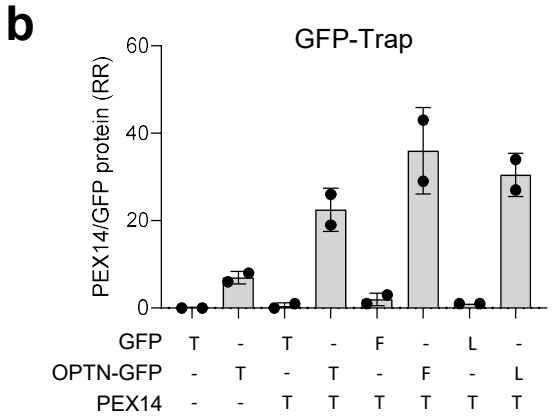

# Extended Data Fig. 4

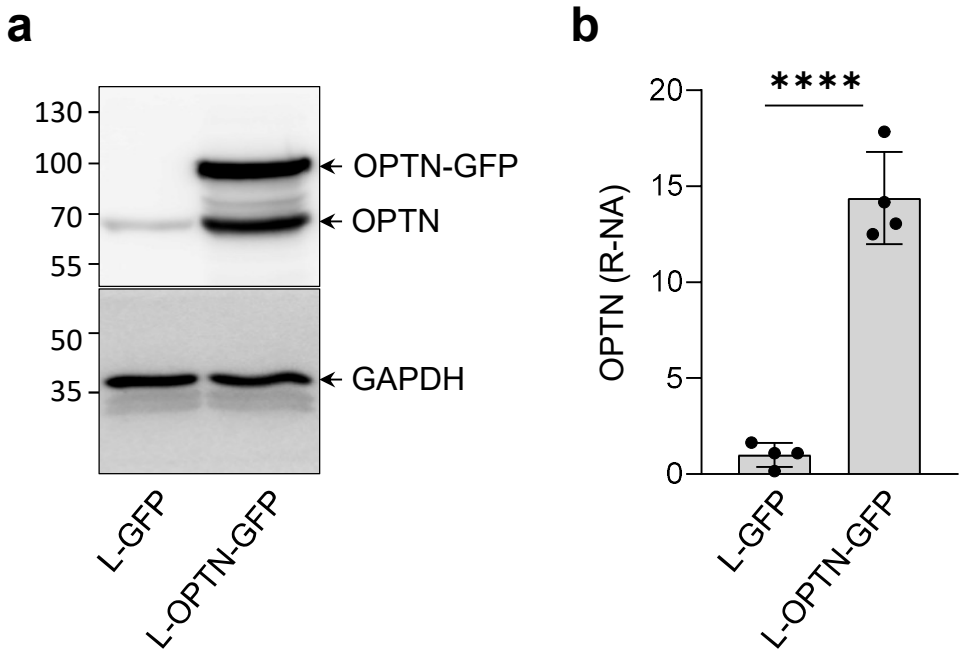

# Extended Data Fig. 5

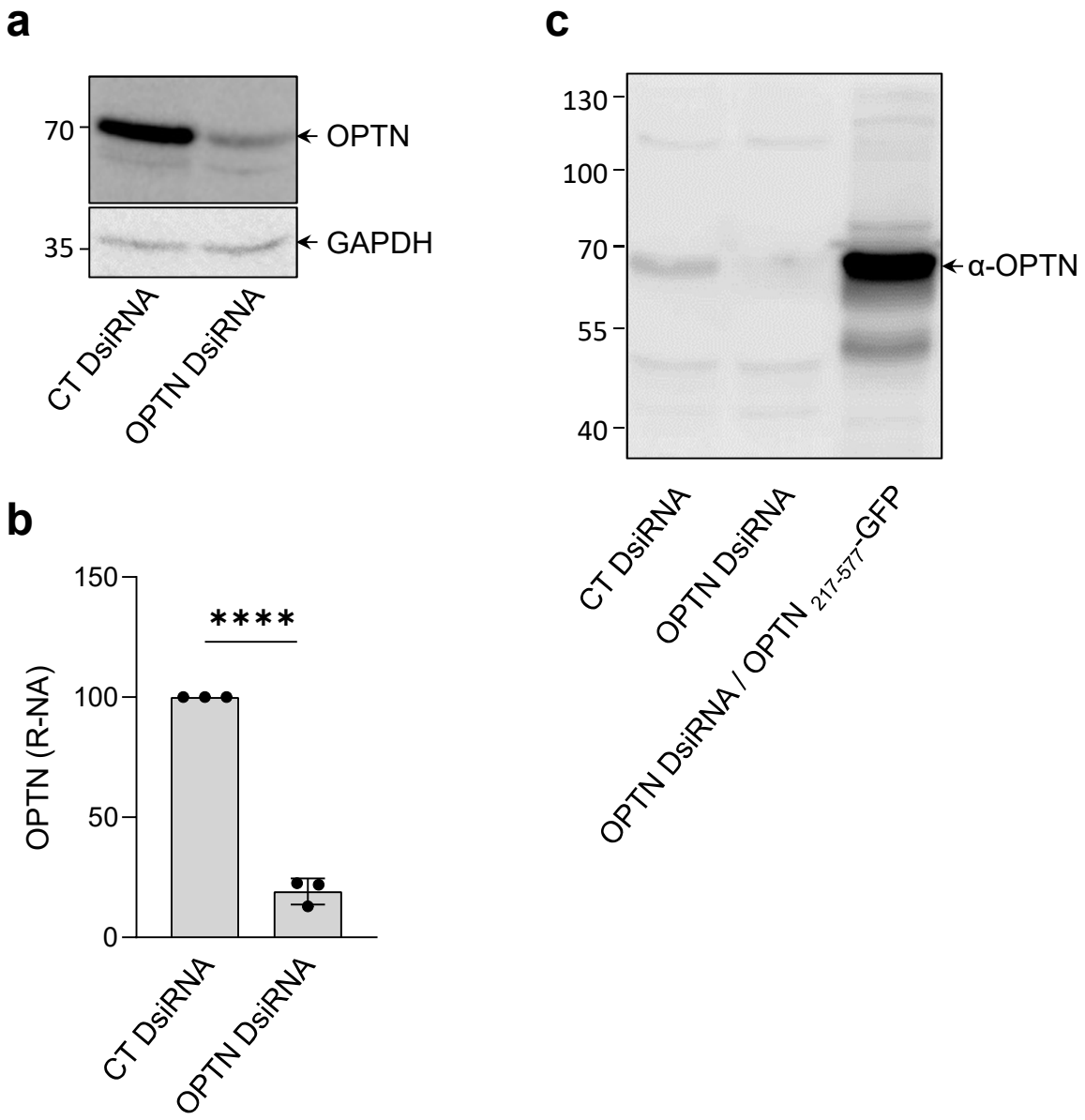

**Extended Data Fig. 6**

**a**

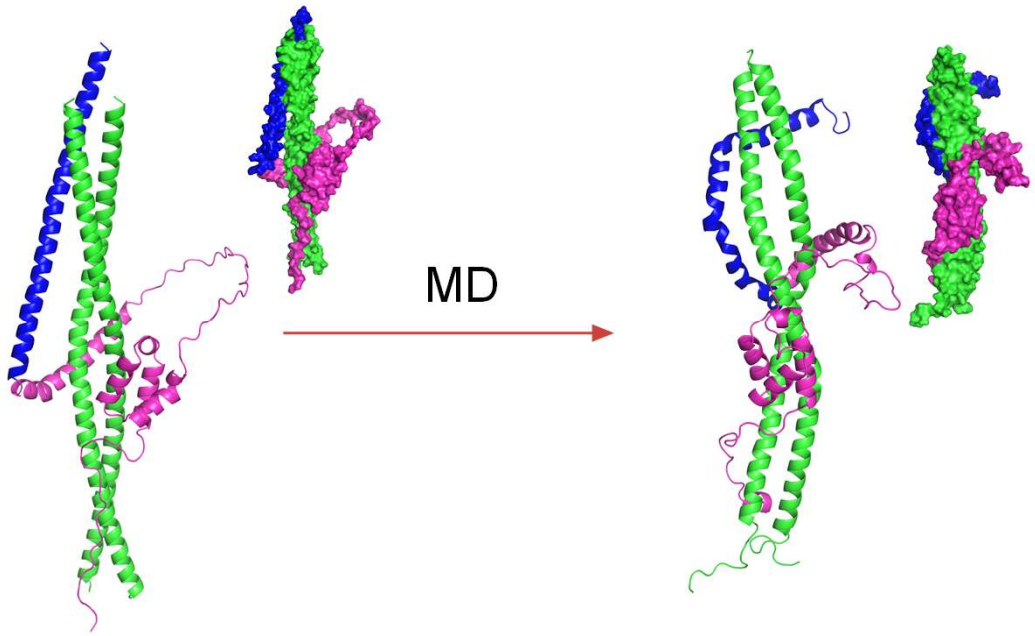


**b**

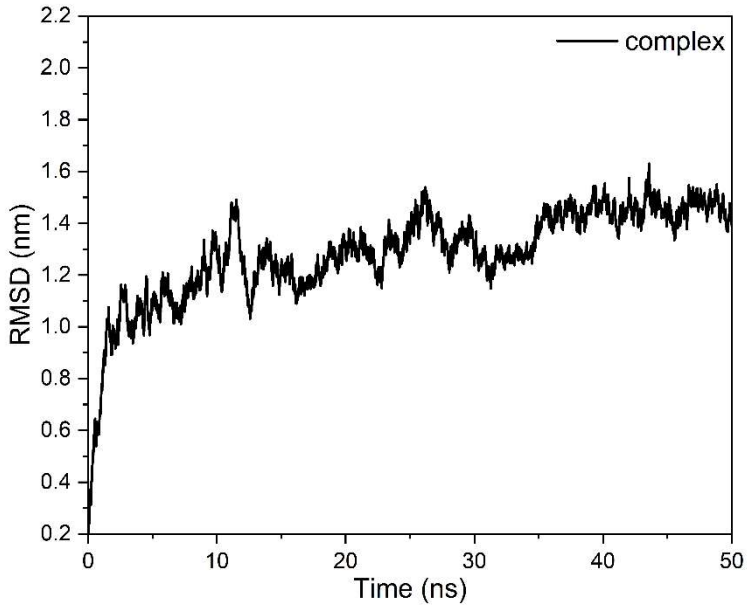

# Extended Data Fig. 7

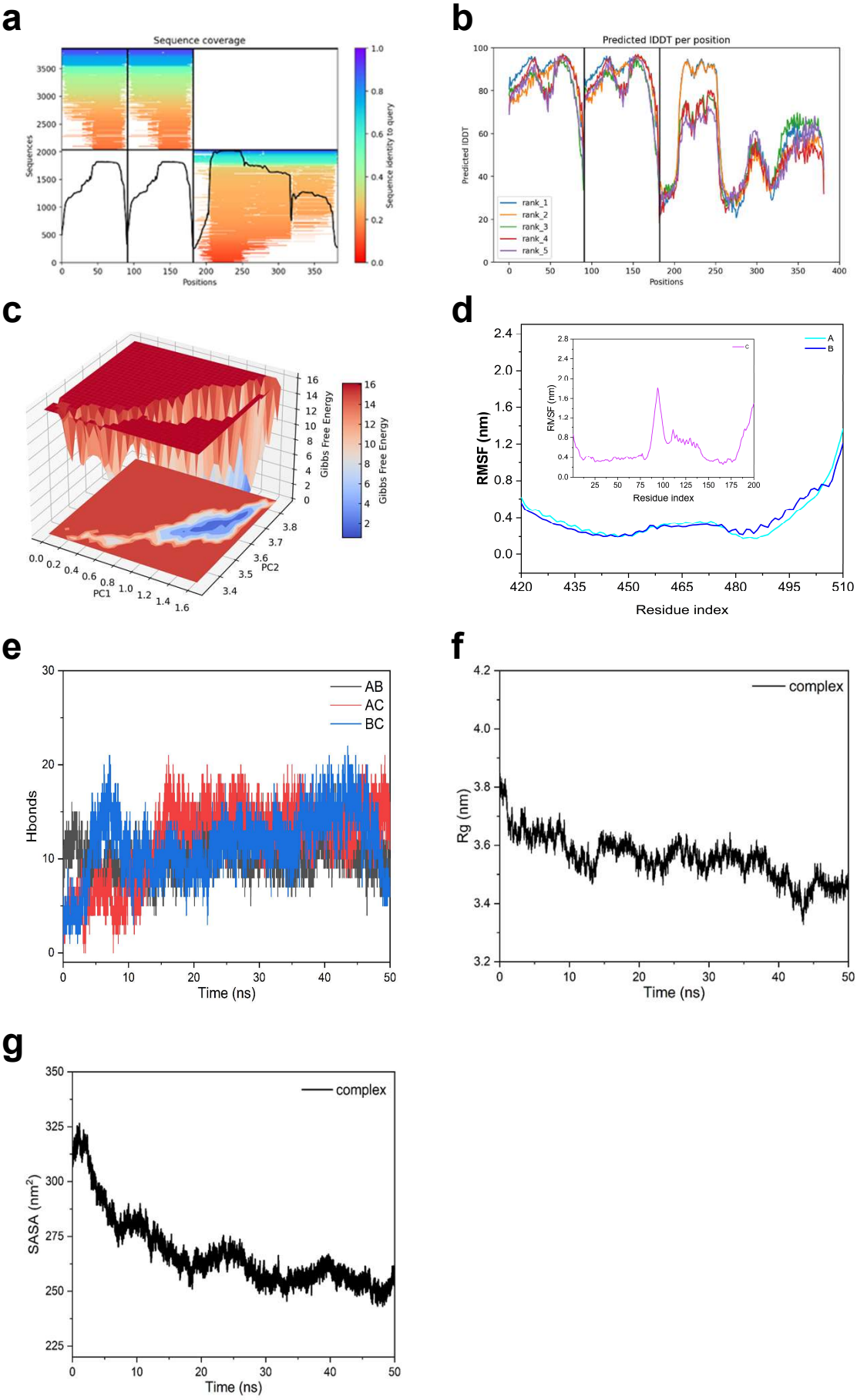

# Extended Data Fig. 8

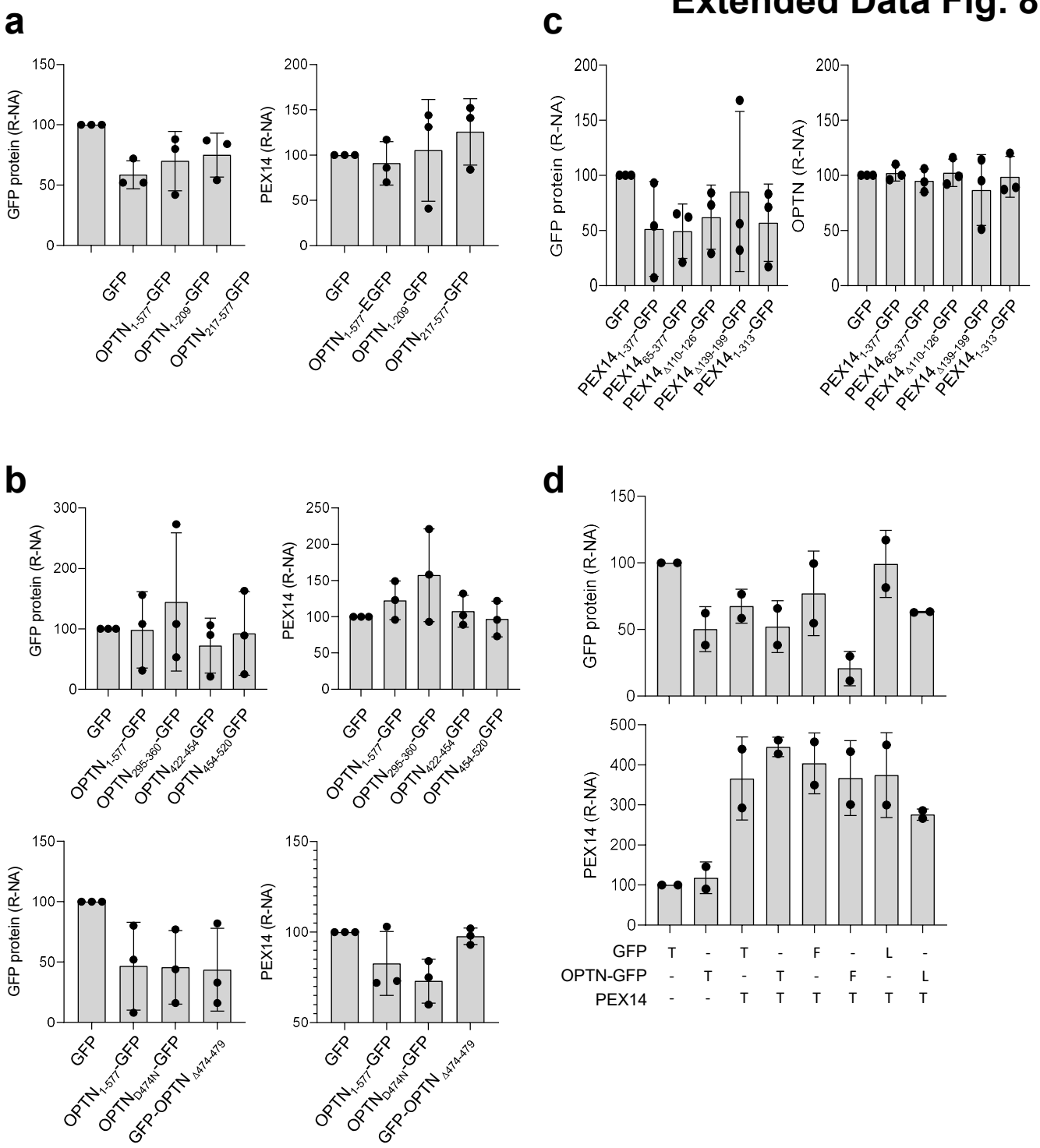

# Extended Data Table 1

| Complex | A-B | A-C | B-C |
|---|---|---|---|
| ΔEvdw | -224.88+/-5.9 | -110.57+/-7.04 | -202.83+/-3.78 |
| ΔEele | -41.54+/-4.1 | -64.38+/-6.05 | -45.56+/-7.11 |
| ΔGGB | 40.02+/-3.31 | 63.06+/-5.11 | 49.54+/-6.76 |
| ΔGSA | -33.77+/-0.31 | -18.06+/-1.38 | -30.68+/-0.72 |
| ΔGbinding | -257.14+/-7.91 | -129.95+/-10.69 | -229.54+/-10.54 |

# Supplementary Fig. 1

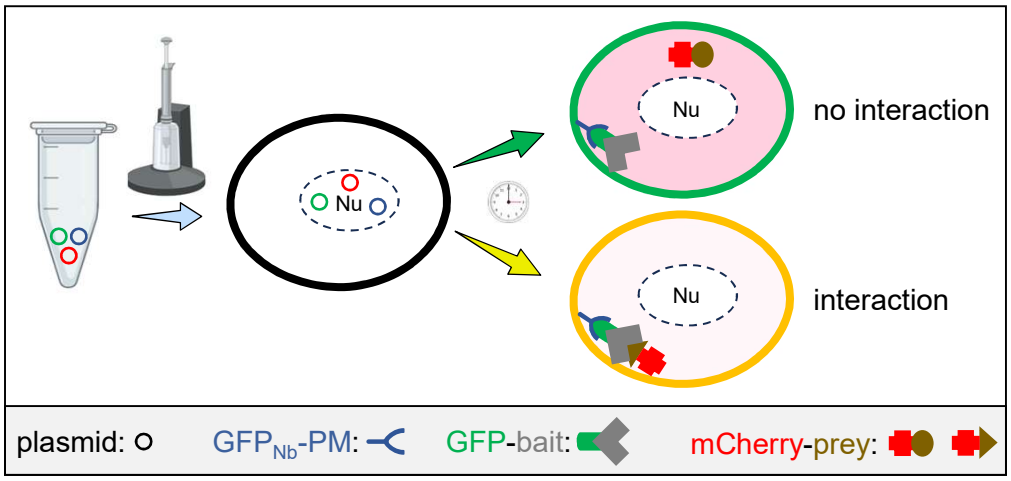

# Supplementary Fig. 2

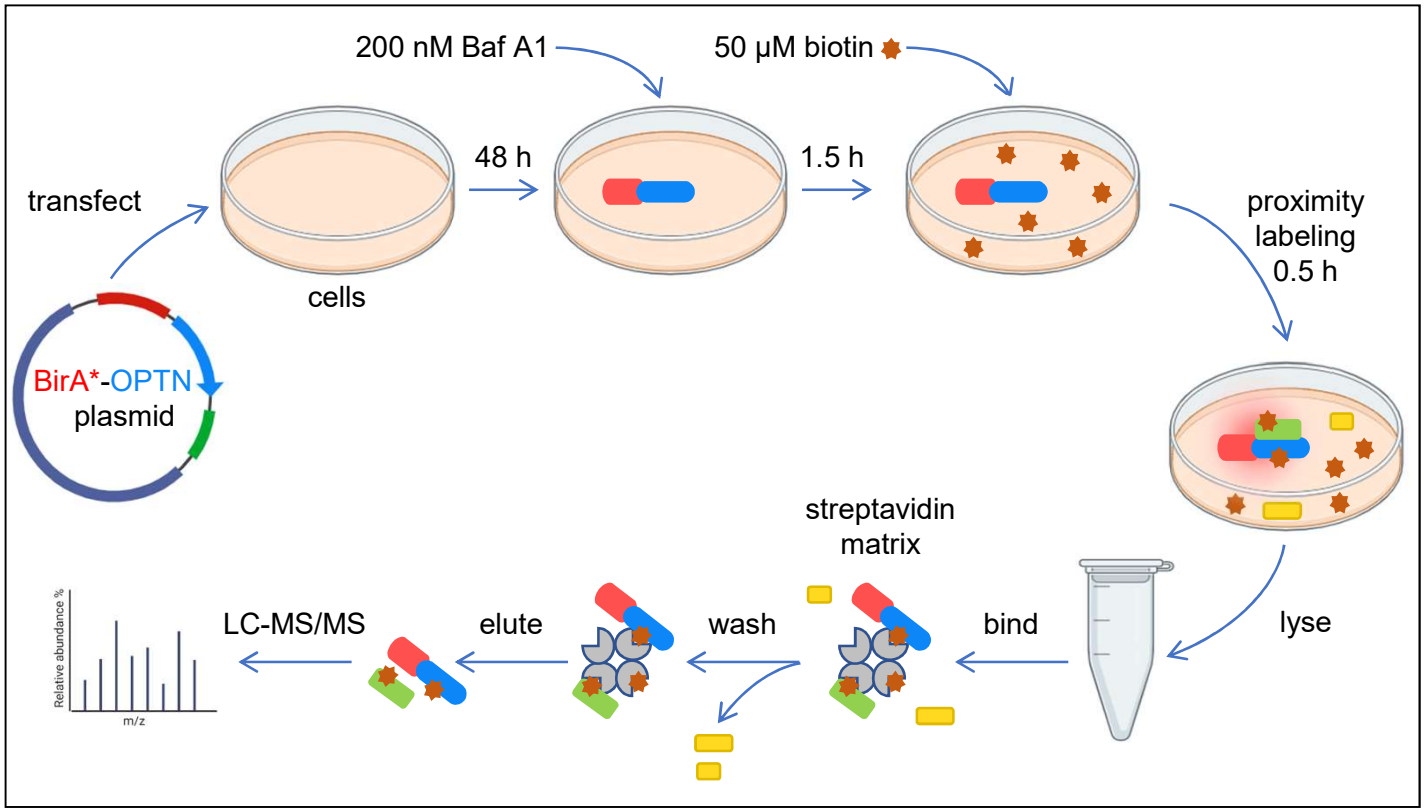

**Supplementary Table 1.** Synthetic oligonucleotide primers used in this study (restriction sites are underlined).

| Name | Nucleotide sequence |
|---|---|
| pDIfw1 | 5’-ggactggctgcatcattcgggatccaatgg-3’ |
| pDIfw2 | 5’-actgttctgcagcgagagagaaaattcatgagg-3’ |
| pDIrv1 | 5’-tgatgcagccagtccctgtcctcagc-3’ |
| pDIrv2 | 5’-tcgctgcagaacagtaaacttccatctgagcc-3’ |
| Pex14.3 | 5’-gggaagatctatggcgtcctcggagcag-3’ |
| Pex14.4 | 5’-aatctgcaggtcccgctcactctcgtt-3’ |
| Pex14.12 | 5’-ggactgcagcacctccatccgcacctg-3’ |
| Pex14.A | 5’-gggaagatctatggccttccagcagtcggg-3’ |
| Pex14.CCfw | 5-atcctgggcggcaccaactggatcctggag-3’ |
| Pex14.CCrv | 5’- gatccagttggtgccgcccaggatgag-3’ |
| Pex14.HDfw | 5’-tggcgagattactacaagaaatacctgctc-3’ |
| Pex14.HDrv | 5’-gtatttcttgtagtaatctcgccatcggga-3’ |
| pHL30Nhelfw: | 5’-cgagcgctagcaccatggcgatcccgc-3‘; |
| pHL30EcoRIRv | 5’-cgagggaattcgcgacccacccgacccgccctttcggcagaccgcag-3’ |
| pHL31Kpn1fw | 5’-cgagggtaccaccatggctatgtcccatcaac-3‘ |
| pHL31Not1Rv: | 5’-cgaggcggccgcttacttgtacagctcgtccatg-3’ |
| pHL32BamHIfw | 5’-gacaccgactctagaggatccaccatggctatgtcccatcaa-3’ |
| pHL32BamHIRv: | 5’-atggtggcgaccggtggatcccgaatgatgcaatccatcacg-3’ |
| pHL34BamHIfw | 5’-cgaggggatccaccatggtgagcgtgatcg-3‘ |
| pHL34SalIRv | 5’-cgagggtcgacttacagcttgctcttgcccag-3’ |
| pHL36fw | 5-gagaaaggcccggagactttagagctacaagtggaaagcatg-3’ |
| pHL36rv | 5’-ccacctgtagctctaaagtctccgggcctttctc-3’ |
| pHL37fw | 5’-gaaaaagtggacagggcagaggacctggaaaccatg-3’ |
| pHL37rv | 5’-catggtttccaggtcctctgccctgtccactttttc-3’ |
| pHL38fw | 5’-aagcaaaccattgccaagcatggggcgagaacaagtgac-3’ |
| pHL38rv | 5’-cctggcaatggtttgcttcatttcatcc-3’ |

**Supplementary Table 2.** Plasmids constructed for this study.

| Name | Protein | Cloning vector | Insert |
|---|---|---|---|
| pDI1 | OPTN$_{\Delta 545-577}$-GFP | Addgene 27052 | Q5 Site-Directed Mutagenesis: template: Addgene 27052 (pDIfw1, pDIrv1) |
| pDI2 | OPTN$_{\Delta 474-479}$-GFP | Addgene 27052 | Q5 Site-Directed Mutagenesis: template: Addgene 27052 (pDIfw2, pDIrv2) |
| pHL30 | miniTurbo-OPTN$_{1-577}$-GFP | Addgene 27052 | NheI/EcoRI-digest of PCR product: template miniTurbo-BirA (pHL30NheIfw, HL30EcoRIRv) |
| pHL31 | OPTN$_{1-577}$-GFP | pcDNA5/FRT/TO vector | KpnI/NotI-digest of PCR product: template Addgene 27052 (pHL31Kpn1fw, pHL31Not1Rv) |
| pHL32 | OPTN$_{1-577}$-GFP | pLenti CMV GFP Puro | BamHI-digest of PCR product: template Addgene 27052 (pHL32BamHIfw, pHL32BamHIRv)[1] |
| pHL34 | po-mKeima | pLenti CMV GFP Puro | BamHI/SalI-digest of PCR product: template pMF2005 (pHL34BamHIfw, pHL34SalIrv)[1] |
| pHL36 | OPTN$_{\Delta 295-360}$-GFP | pEGFP-N1 | BglII/PstI-digest of PCR product: template Addgene 27052 (pHL36fw, pHL36rv)[1] |
| pHL37 | OPTN$_{\Delta 422-455}$-GFP | pEGFP-N1 | BglII/PstI-digest of PCR product: template Addgene 27052 (pHL36fw, pHL36rv)[1] |
| pHL38 | OPTN$_{\Delta 454-520}$-GFP | pEGFP-N1 | BglII/PstI-digest of PCR product: template Addgene 27052 (pHL38fw, pHL38rv)[1] |
| pMF235 | PEX14$_{65-377}$-GFP | pEGFP-N1 | BglII/PstI-digest of PCR product: template 120 (Pex14.A, Pex14.4) |
| pMF415 | PEX14$_{1-313}$-GFP | pEGFP-N1 | BglII/PstI-digest of PCR product: template 120 (Pex14.3, Pex14.D) |
| pMF663 | PEX14$_{\Delta 139-199}$-GFP | pEGFP-N1 | BglII/PstI-digest of fusion PCR product: template 120 (primer set 1: Pex14.3, Pex14.CCrv; primer set 2: Pex14.4, Pex14.CCfw) |
| pMF682 | PEX14$_{\Delta 110-126}$-GFP | pEGFP-N1 | BglII/PstI-digest of fusion PCR product: template 120 (primer set 1: Pex14.3, Pex14.HDrv; primer set 2: Pex14.4, Pex14HDfw) |

[1] The PCR product was treated with DpnI and then inserted into the cloning vector using the NEBuilder HiFi DNA Assembly cloning kit.